

# Developing an Integrated Petrogenetic Model for Understanding REE Depletion of the Ampasibitika Intrusion and Associated Ion Adsorption Deposits

E. Marquis<sup>1</sup>\*, K. M. Goodenough<sup>2</sup>, M. P. Smith<sup>3</sup>, G. Estrade<sup>4</sup>, F. Rasolonirina<sup>5</sup> and R. L. Rakotoson<sup>5</sup>

<sup>1</sup>Camborne School of Mines, Department of Earth and Environmental Sciences, University of Exeter, Penryn Campus, Cornwall TR10 9EZ, United Kingdom

<sup>2</sup>British Geological Survey, The Lyell Centre, Edinburgh EH14 4AP, United Kingdom

<sup>3</sup>School of Applied Sciences, University of Brighton, Brighton BN24GJ, United Kingdom

<sup>4</sup>Géosciences Environnement Toulouse, Observatoire Midi-Pyrénées 14, avenue Édouard Belin 31400 Toulouse, France

<sup>5</sup>Antananarivo, Madagascar

\*Corresponding author. Telephone: 01326 370400. E-mail: e.marquis@exeter.ac.uk.

## Abstract

Alkaline–peralkaline igneous systems are promising sources of rare earth elements (REEs). Preservation bias has resulted in a gap in the geological record for alkaline–peralkaline magmatic systems, with the hypabyssal plumbing system linking magma chambers to extrusive volcanic rocks poorly represented. Large plutonic varieties of these systems are often proposed to have fed (now eroded) volcanoes, and current peralkaline volcanic systems obscure the plutonic system at depth. The alkaline to peralkaline Ampasibitika Intrusion in Madagascar is a rare example where the magmatic–volcanic interface between a deeper level magma reservoir and its genetically related caldera volcano is exposed. This c. 24 Ma sub-volcanic intrusive system comprises silica-undersaturated to silica-oversaturated units, of peralkaline to metaluminous and peraluminous characters, with varying styles of REE mineralisation, including supergene ion adsorption-style REE occurrences in the overlying weather profiles. There are two main intrusive suites: (1) the concentric Marginal Dyke Swarm (MDS) formed of quartz–microsyenite and peralkaline granite dykes (PGDs), and (2) the Ampasibitika Ring Dyke (ARD) comprising alkali feldspar syenites and subordinate nepheline syenites, trachytes and phonolites. We present new field observations and geochemical data to indicate that the MDS was emplaced as a series of low-viscosity, volatile-rich melt batches, which coalesced in the magma reservoir roof zone and intruded prior to caldera collapse, whereas the ARD was emplaced into the ring fault as a heterogeneous mix of variably evolved syenitic crystal mushes and phonolitic to trachytic-melt batches. As such, we suggest the MDS represents the residual melt fraction of the magma reservoir, whereas the ARD contains portions of the fractionating, silica-neutral to silica-undersaturated syenite, cumulate assemblage. In this revised framework, we assess the major and trace element geochemistry of amphibole- and clinopyroxene-group minerals to gain insight into the magmatic evolution of the Ampasibitika Intrusion and partitioning of REE between early cumulate and residual melt phases. Ultimately, the most REE-enriched units, the PGDs of the MDS, are identified as the product of the most volatile-rich, highly evolved melts from the roof zone of the magma reservoir. However, although REE enriched, the mineralogy does not always enable efficient release of REE for ion adsorption-style mineralisation; instead, lower REE-content protoliths with REE-host phases more amenable to decomposition release a greater proportion of REE.

**Keywords:** peralkaline, hypabyssal, rare earth elements, depletion, ion adsorption deposits, petrogenesis

## INTRODUCTION

Rare earth elements (REEs) are widely classified as critical raw materials (European Commission, 2020; Lusty *et al.*, 2021; US Geological Survey, 2022). This classification stems from their extensive use in decarbonised energy and transport systems, coupled with the dominance of a single country (China) across all aspects of their supply chain (Goodenough *et al.*, 2018; European Commission, 2020). The majority of REE resources are associated with carbonatites and alkaline–silicate rocks, with commercial production dominantly from carbonatite-hosted, placer and ion adsorption deposits (IADs) (Sanematsu & Watanabe, 2016). The latter are the weathering products of felsic igneous rocks and are the primary source of the world's heavy REE (HREE) (Bao & Zhao, 2008; Jowitt *et al.*, 2017; Jowitt, 2018; Li *et al.*, 2019; Beard *et al.*, 2022).

Despite currently limited production, alkaline–peralkaline silicate igneous systems are promising sources of future REE supply (e.g. Smith *et al.*, 2016; Marks & Markl, 2017; Goodenough *et al.*, 2018; Beard *et al.*, 2022). Peralkaline rocks are volcanic to plutonic rocks containing an excess of alkalis relative to aluminium ( $([Na + K]/Al > 1)$ ; Le Maitre *et al.*, 2002). Peralkaline rocks are divided into agpaitic and miaskitic varieties; the former host REE and high-field-strength elements (HFSE) in complex Na/K–Ca–HFSE minerals, whereas in the latter, these elements are hosted in ‘simple’ phases such as zircon and titanite (Marks & Markl, 2017). Geo-metallurgical challenges related to the processing of agpaitic minerals mean that, at present, REE and HFSE deposits associated with alkaline–peralkaline silicate systems struggle to be economic (Goodenough *et al.*, 2018; Beard *et al.*, 2022).

Received: January 24, 2023. Revised: June 2, 2023. Accepted: June 21, 2023

© The Author(s) 2023. Published by Oxford University Press.

This is an Open Access article distributed under the terms of the Creative Commons Attribution License (<https://creativecommons.org/licenses/by/4.0/>), which permits unrestricted reuse, distribution, and reproduction in any medium, provided the original work is properly cited.

As noted by Beard *et al.* (2022), linking alkaline–silicate volcanism to mineralised alkaline–silicate plutonic systems is challenging due to extensive erosion of volcanic and hypabyssal sequences. There has been significant research on alkaline–silicate plutonic systems, such as the llímaussaq, Puklen, Ivigtut, and Motzfeldt complexes of the Gardar Igneous Province (Goodenough *et al.*, 2000; Marks & Markl, 2003; Schonenberger & Markl, 2008; Marks & Markl, 2015; Borst *et al.*, 2016), the Strange Lake complex (Salvi & Williams-Jones, 1996; Salvi & Williams-Jones, 2006; Siegel *et al.*, 2018) and the Blatchford Lake complex, which includes the Nechalacho Layered Suite, of Canada (Möller & Williams-Jones, 2016a; Möller & Williams-Jones, 2016b). In contrast there are relatively few well-documented caldera systems described (e.g. Ambohimirahavavy Complex, Madagascar—Estrade *et al.*, 2014a; Poços de Caldas Alkaline Complex, Brazil—Schorscher & Shea, 1992; Pilanesberg Complex, South Africa; Cawthorn, 2015; Andersen *et al.*, 2017; Elburg & Cawthorn, 2017). In the absence of direct observation of plutonic volcanic connection in alkaline systems, it is difficult to predict where mineralised systems might occur at depth.

In addition, a particular feature of REE-mineralised systems is the potential for weathering to improve the economics of the deposits (e.g. Mt. Weld carbonatite, Australia, Lottermoser, 1990; Zhukova *et al.*, 2021; Zudong granite, China; Li *et al.*, 2019). Ion-adsorption deposits are lateritic regolith-hosted REE ores typically derived from the weathering of alkaline granites, with the best-known examples in South China (e.g. Sanematsu & Watanabe, 2016; Li *et al.*, 2017). These ores are defined as containing over 50% of their REE adsorbed to clay minerals and are thus easily extractable using solvent ion exchange techniques (e.g. Ruan *et al.*, 2005; Moldoveanu & Papangelakis, 2012; Moldoveanu & Papangelakis, 2013; Tian *et al.*, 2013; Moldoveanu & Papangelakis, 2016). Although IADs are low-grade deposits, generally containing 0.05 to 0.38 wt % REO (Li *et al.*, 2017), cut-off grades of 0.06 to 0.15 wt % REO are acceptable due to the ease of extraction (Ding & Deng, 2013; Li *et al.*, 2017). Although weathering and eluviation–illuviation processes are important for the development of weathered phases and REE accumulation in these deposits, it is the magmatic and hydrothermal processes involved in the development of the protolith that dictate the primary REE-host mineralogy and therefore the REE pattern of the regolith (Li *et al.*, 2017; Xu *et al.*, 2017; Estrade *et al.*, 2019; Li *et al.*, 2019).

The research presented here is part of the SoS RARE project, which aimed to determine if lateritic regolith profiles developed over a REE-mineralised alkaline–peralkaline silicate system would produce IAD ores of higher REE grade. The Ampasibitika Intrusion of northwestern Madagascar was chosen as the natural laboratory for this study, due to the combination of REE-mineralised alkaline–peralkaline rocks (Estrade *et al.*, 2014b; Estrade *et al.*, 2019) and the presence of regolith-hosted ion exchangeable REE (Desharnais *et al.*, 2014; Borst *et al.*, 2020). Understanding the mineralogical evolution of the complex is a vital part of developing a geological model for this type of deposit.

In this paper, we further refine the magmatic evolution and emplacement model of this intrusion and suggest how this influences the subsequent development of IADs. In particular we (1) determine the emplacement style and relative timing for different components of the Ampasibitika Intrusion and (2) use bulk rock and amphibole- and clinopyroxene-group major and trace element chemistry to gain insight into the early and late magmatic processes taking place in the parental magma reservoir and on emplacement to shallow crustal levels, and (3) in the framework of this refined evolution model, we discuss the possible mech-

anisms by which cogenetic agpaitic silica-undersaturated and silica-oversaturated melts may form.

## GEOLOGICAL SETTING

Madagascar is the amalgamation of a series of Archaean to Neoproterozoic cratonic and arc terranes, which were juxtaposed during the Pan-African Orogeny in the late Neoproterozoic to Cambrian (Collins & Pisarevsky, 2005; Collins, 2006; Key *et al.*, 2011; Armistead *et al.*, 2019; Armistead *et al.*, 2020). In the northwest of Madagascar, the Proterozoic arc terranes of the Bemarivo Belt and the Archean Antananarivo Craton are juxtaposed along the Sandrakota Shear Zone (SSZ) (Thomas *et al.*, 2009; Armistead *et al.*, 2019). Mesozoic to Cenozoic sedimentary units, deposited in basins during the rifting of Madagascar from Africa, drape the western margin of the island (Wit, 2003; Papini & Benvenuti, 2008).

Northern Madagascar has been affected by multiple magmatic episodes since the Pan-African Orogeny: (1) post-collisional emplacement of the Maevarano Suite granitoids (c. 537–522 Ma) (Goodenough *et al.*, 2010), (2) Late Cretaceous tholeiitic flood basalt volcanism (c. 92–86 Ma) (Melluso *et al.*, 2001), and (3) Cenozoic to recent, alkaline to peralkaline, intrusive to extrusive magmatism (e.g. Melluso *et al.*, 2007a, 2007b; Tucker *et al.*, 2008; Cucciniello *et al.*, 2011, 2016). The latter includes the Ampasindava Alkaline Province that consists of a series of alkaline to peralkaline, intrusive to extrusive complexes, generally aligned NW–SE along the SSZ (Tucker *et al.*, 2008; Estrade *et al.*, 2014a). Although historically proposed to be related to hotspot activity (Emerick & Duncan, 1982), the development of low-degree partial melts in the region is now considered to be related to decompression melting of metasomatized lithospheric mantle in response to Cenozoic crustal extension (Melluso *et al.*, 2007a; Melluso *et al.*, 2007b; Cucciniello *et al.*, 2011; Rocco *et al.*, 2013; Estrade *et al.*, 2014a; Cucciniello *et al.*, 2016; Rocco *et al.*, 2017). There is a strong structural control on the distribution of alkaline complexes in northern Madagascar, with alignment of complexes parallel to the NW–SE SSZ and conjugate fault sets (Fig. 1a) (Melluso *et al.*, 2007b; Estrade *et al.*, 2014a), indicating channelling of melts along reactivated old lithospheric fractures (Nougier *et al.*, 1986; Estrade *et al.*, 2014a).

The Ambohimirahavavy alkaline complex is elongated along its NW–SE axis (Fig. 1a, b), and mafic dykes cross-cutting the complex are parallel to sub-perpendicular to the axis (i.e. NW–SE to NNE–SSW; Fig. 1b), supporting a structural control on melt emplacement. The complex intrudes Mesozoic basin-fill sediments of the Isalo Group, dominated by marls and claystone with subordinate sandstones, and interspersed with limestones (Papini & Benvenuti, 2008). First described in detail by Lacroix (1902), the diversity of intrusive lithologies, and development of agpaitic mineral assemblages, has attracted geologists studying the development of cogenetic silica-oversaturated and silica-undersaturated peralkaline rocks (Donnot, 1963; Ganzev *et al.*, 1989; Estrade *et al.*, 2014a) and the occurrence of REE mineralisation (Ganzev & Grechishchev, 2003; Desharnais *et al.*, 2014; Rakotovo *et al.*, 2014; Estrade *et al.*, 2014b). Two intrusions make up the complex. To the northwest, the Tsarabariabe Intrusion comprises several syenitic and subordinate biotite granite centres variably covered by tuffs and volcanic breccia. Whereas to the southeast, the Ampasibitika Intrusion forms a distinctive caldera filled with extrusive volcanic rocks surrounded by a circular ridge underlain by syenites, interpreted as a ring dyke (Estrade *et al.*, 2014a). Due to better accessibility and known development of ion

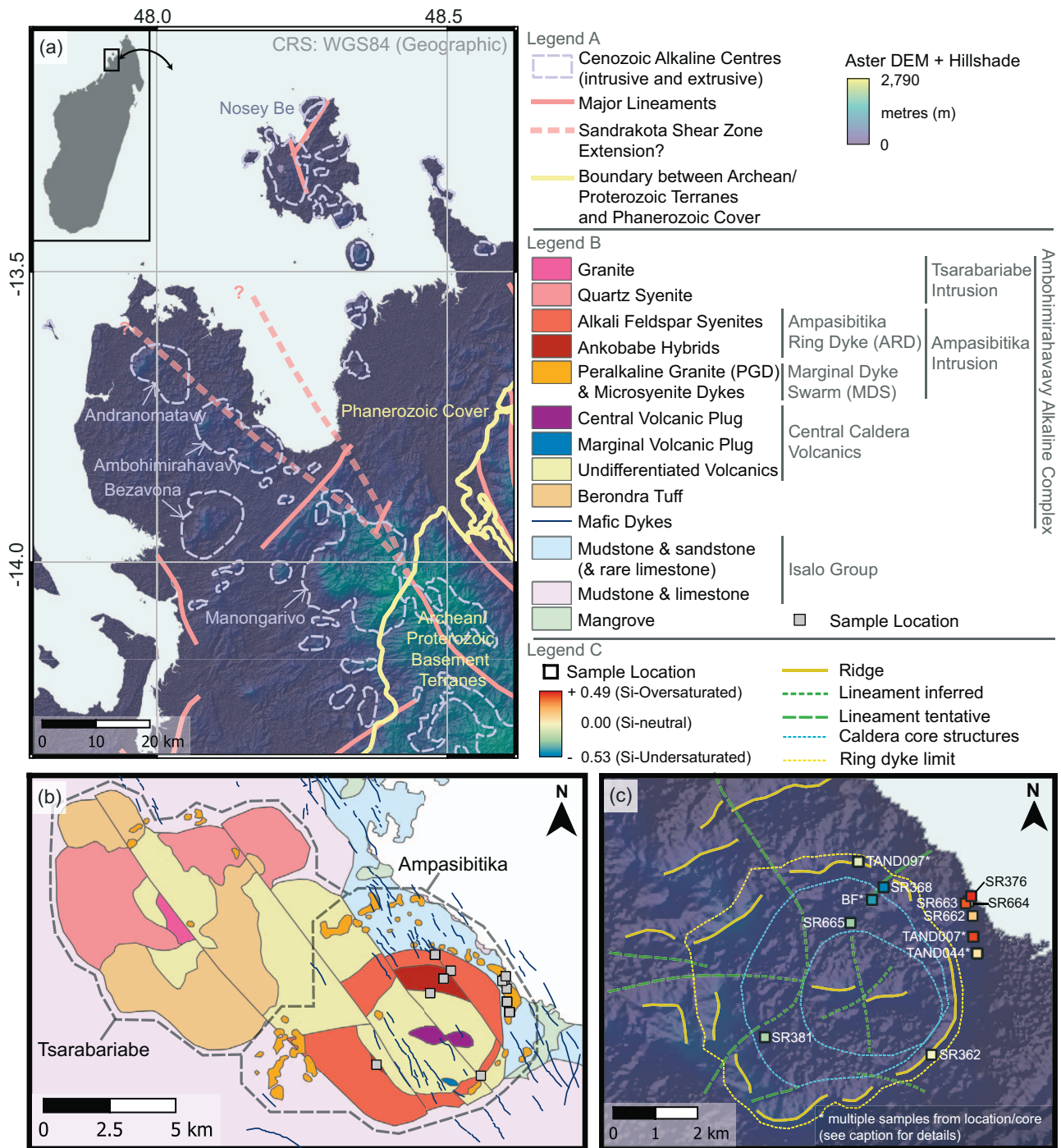


**Fig. 1.** (a) Map showing the topographic variation (ASTER GDEM), major faults and terrane/cover boundaries across the Ampasindava Peninsula and the surrounding region. The exact extension of the SSZ to the NW is obscured by the Phanerozoic cover; possible extensions of the SSZ are indicated by the pale red dashed line. Inset shows the position of the area in relation to Madagascar. (b) Geological map of the Ambohimirahavavy Alkaline Complex adapted from Estrade *et al.* (2014a) and amended with field observations. (c) Topographic map (ASTER GDEM) of the Ampasibitika Intrusion illustrating inferred linear features of the caldera structure present, including ridge underlain by ring dyke (Estrade *et al.*, 2014a) and caldera collapse structures. Locations of samples analysed in this study are shown. Labels with the prefix 'SR' represent individual samples, the prefix 'TAND' represents locations of cores from which multiple samples were analysed, and 'BF\*' represents the 'Ankobabe Boulder Field' site from which the nepheline syenite and magma mingling samples were collected.

adsorption REE mineralisation, the Ampasibitika Intrusion is the focus of this study.

The Ampasibitika Intrusion is c. 7 km in diameter, outcropping from 0 to c. 700 m above sea level. Previous studies have classified this intrusive to extrusive centre as a caldera surrounded by an annular ring dyke (Estrade *et al.*, 2014a). Hillshade models from

ASTER GDEM digital elevation models (ASTER GDEM, 2011) further highlight this structure (Fig. 1a, c). Qualitative interpretation of the hillshade model indicates the presence of several linear structures intersecting the caldera and ring dyke. Features include annular structures interpreted to be caldera depressions and surrounding ring dyke (defined by the elevated ridge surrounding

the central caldera depression), cross-cutting linear valleys/depressions inferred to represent caldera and trans-caldera faults. These structures are consistent with fault structures developed during piece-meal caldera collapse (e.g. Troll *et al.*, 2002).

Intrusive units of the Ampasibitika Intrusion include both agpaitic nepheline syenites and granites, plus multiple other silica-undersaturated to silica-oversaturated peralkaline, metaluminous and peraluminous rocks. The proximity of intrusive and extrusive phases indicates that this intrusion spans the magmatic–volcanic interface. It has been recognised that to develop co-genetic silica undersaturation and oversaturation in the Ampasibitika Intrusion, contamination of a parental silica-undersaturated melt is required (Estrade *et al.*, 2014a). However, the timing and extent of this contamination remains uncertain.

The ring dyke of the Ampasibitika Intrusion comprises alkali feldspar syenites, and subordinate nepheline syenites that are restricted to the dyke's inner margin (Fig. 1b) (Estrade *et al.*, 2014a). Estrade *et al.* (2014a) described four syenite variants: (1) quartz alkali feldspar syenite, (2) alkali feldspar syenite, (3) type 1 nepheline syenite and (3) type 2 nepheline syenite.

Isalo Group sedimentary rocks on the outer flanks of the annular escarpment are intruded by a discontinuous series of quartz–microsyenite and peralkaline granite dykes (PGDs); these dykes are up to 10 m wide and are typically orientated parallel to the main ring dyke (Estrade *et al.*, 2014a). Estrade *et al.* (2014a, 2014b) classified PGDs into three varieties: (1) GR-I, a homogeneous medium- to coarse-grained miaskitic granite, comprising alkali feldspar, quartz, and arfvedsonite and/or aegirine; (2) GR-II, termed 'fasibitkites' by Lacroix (1915), agpaitic to miaskitic granites comprising alkali feldspar, quartz, arfvedsonite and/or aegirine, zircon and other accessory HFSE phases, and varying internally from pegmatitic to aplitic, with finer scale banding in aplites resulting from changes in modal mineralogy; and (3) GR-III, agpaitic granitic pegmatites with banded aplitic textures that are rich in eudialyte group minerals (EGMs), aegirine and leakeite. REE-mineralised skarns have developed where PGD intruded limestones of the Isalo Group (Estrade *et al.*, 2015).

Heterogeneous volcanic breccias, rhyolitic obsidian volcanic plugs and nepheline microsyenite dykes fill the central caldera (Estrade *et al.*, 2014a). Such shallow-level extrusive volcanic units are absent from the outer flanks of the Ampasibitika Intrusion (Fig. 1b).

## FIELD OBSERVATIONS

Developing a detailed overview of intrusive relationships within the Ampasibitika Intrusion is challenging due to the limited outcrop. Regolith of variable thickness (0 to 30 m) covers the area. Outcrop is restricted to river valleys and rare escarpments. Boulder fields are common and provide good sampling opportunities, especially where boulders are proximal to ridge crests and thus inferred to be close to their origin. Cores from diamond drilling across the area enable infilling of geology where surface outcrops are lacking. In this section, we build on previous work to describe our new field observations including lithologies and textural relationships. We divide the Ampasibitika Intrusion into three main components:

- Central caldera volcanics, comprising heterogeneous volcanoclastic units plus phonolite and trachyte volcanic plugs located within the bounds of the main ring dyke structure;

- Ampasibitika Ring Dyke (ARD), the main ring dyke structure predominantly containing alkali feldspar and nepheline syenites (Estrade *et al.*, 2014a), with minor dykes and enclaves;
- Marginal Dyke Swarm (MDS), a series of quartz–microsyenite to granitic dykes intruding the outer flanks of the Ampasibitika Intrusion in parallel to the ARD. This encompasses the PGD described by Estrade *et al.* (2014a, 2014b).

The majority of ARD syenites are medium to coarse grained, although there is variability of grain size within the samples. Very coarse-grained to pegmatoidal decimetre-scale patches occur sporadically within core sections and outcrop. In addition, some syenites contain interstitial microcrystalline (<0.5 mm) assemblages within coarser-grained frameworks, and in several instances aplitic bands cross-cut syenites.

Alkali feldspar syenites were observed in saprolite at the apex of the ARD ridge (see Estrade *et al.*, 2019) and in core TAND097 located on the outer NE flank of the ARD. This core intersects weathered syenite from 0 to ~8 m down the hole. Below that the core intersects heterogeneous alkali feldspar syenite until the end of the hole at ~69 m.

Occurrences of nepheline syenite were studied in the Ankobabe Boulder Field (Fig. 1c) and a stream on the inner SW flank of the ring dyke (SR381; Fig. 1c). Medium-grained nepheline syenites are variably cross-cut by fine phonolite dykes or contain trachytic-phonolite enclaves (Fig. 2a–c). Phonolite dykes are typically 15 to 30 cm wide and have irregular contacts with host syenites. Thin (<0.5 cm) green microcrystalline veins locally cross-cut nepheline syenites. Enclaves have sharp (Fig. 2a) to diffuse (Fig. 2b) contacts with the surrounding nepheline syenites and are lobate (Fig. 2a–b) to angular (Fig. 2c) in geometry. These range in diameter from ~2 to >25 cm. Both phonolite dykes and trachytic-phonolite enclaves contain alkali feldspar fragments and laths, interpreted as xenocrysts as they appear to have been plucked from the surrounding syenitic host rock and often exhibit fragmented textures or evidence of resorption. These xenocrysts indicate that emplacement occurred when a crystal network had begun to form but crystallisation was incomplete. Some of the more lobate enclaves (Fig. 2b) contain amoeboid to elliptical leucocratic blebs (~1 cm in width). This heterogeneous assemblage is henceforth termed the Ankobabe Hybrids.

On the outer flanks of the Ampasibitika Intrusion, mudstone, marl, limestone and sandstone units of the Isalo Group are sporadically intruded by the laterally discontinuous quartz–microsyenite and PGD dykes of the MDS (Fig. 2d–f). These dykes range from 5 to 3 m thick and strike parallel to and dip gently (<10°) towards the main ARD (Fig. 2e). Some quartz–microsyenite dykes are classified as trachytic due to the presence of phenocrysts and flow banding. Granitic dykes exhibit a range of textures, from equigranular to banded aplitic and pegmatite, as described by Estrade *et al.* (2014a, 2014b). Contacts between dykes and the country rock are sharp with chilled margins, and the degree of alteration of the host rock is highly variable (Fig. 2f). Contacts between granitic and quartz–microsyenite dykes are observed in the core but do not conclusively demonstrate age relationships between the different dyke compositions (Fig. 2d).

## METHODS

During this project, further mapping of the Ampasibitika Intrusion was integrated with previous studies (e.g. BGS-USGS-GLW, 2008; Estrade *et al.*, 2014a); 30 samples of intrusive units from the diamond drill core and field exposure were collected for chem-

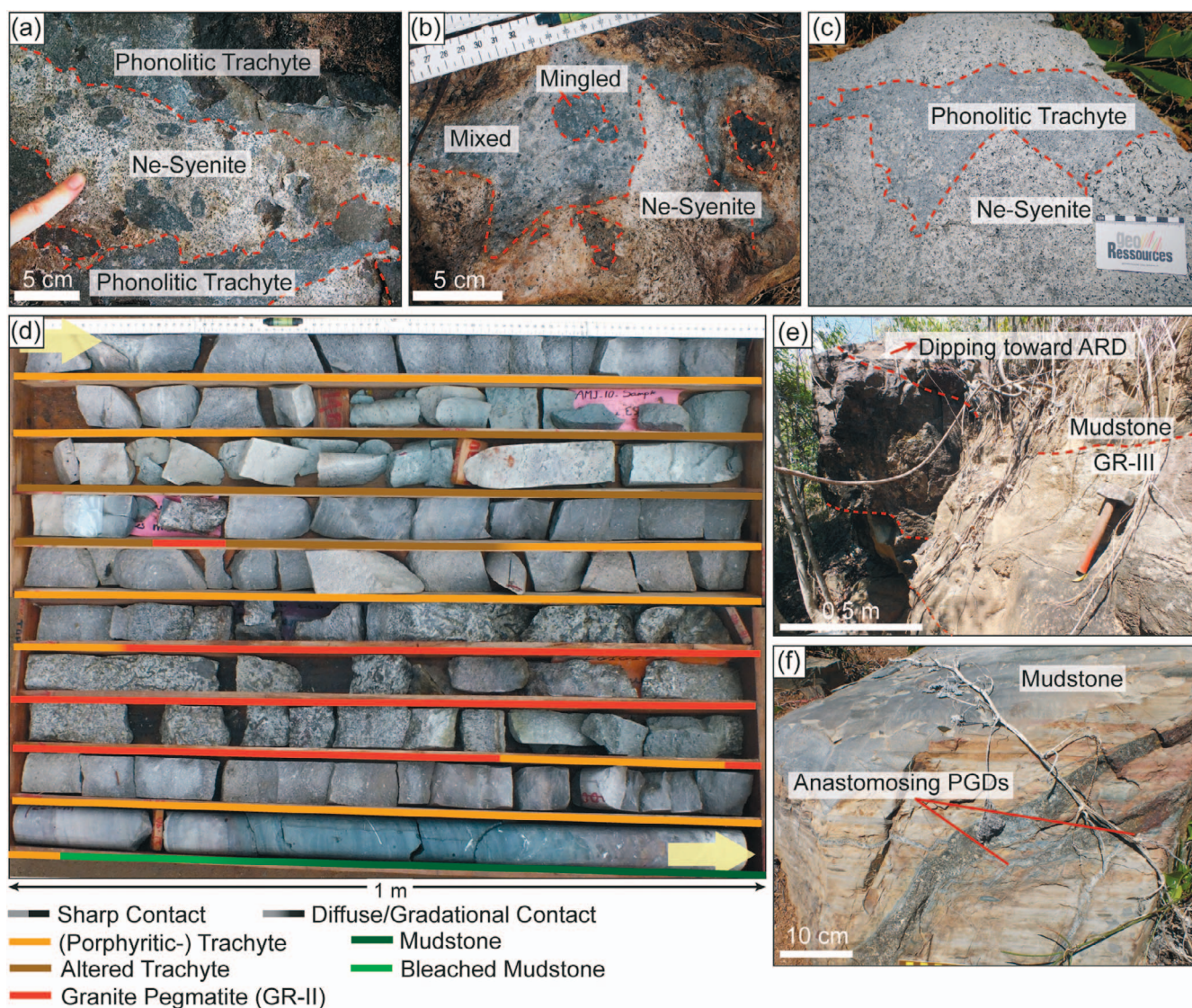


**Fig. 2.** Field relationships. Panels a–c illustrate magma mixing to mingling textures observed in boulders located in the Ankobabe Boulder Field (inner northern flank of the ARD): (a) lobate enclaves of discrete phonolitic trachyte hosted with nepheline syenite, (b) variably homogenised, mixed to mingled, interaction between phonolitic trachyte and nepheline syenite and (c) angular enclave of phonolitic trachyte, containing xenocrysts and xenoliths of host nepheline syenite. (d) Diamond drill core TAND044 located on the outer eastern flank of the Ampasibitka Intrusion and intersection trachyte and peralkaline granite units of the MDS. (e) GR-II type PGD located on the outer eastern flank dips gently towards the ARD. This dyke has a banded texture with quartz lenses, and aplitic to coarse-grained granular layers; it has a sharp contact with the host mudstone with sporadic dykelets (<1 cm wide) off shooting from the main dyke. (f) GR-II type dyke hosted in layered mudstone with complex intrusion geometry and off shooting dykelets, consistent with the low-viscosity nature of the granitic melts (Estrade *et al.*, 2014b).

ical analysis. Samples containing enclaves or a dyke material within the host rock material were separated and analysed separately (e.g. sample SR665 split into SR665-1 trachytic-phonolite enclave and SR665-2 nepheline syenite host). Some lithologies, notably the PGDs, are heterogeneous, and samples taken were as large as possible to account for this heterogeneity. Bulk rock geochemical data for major oxides was analysed by ALS, Co., Galway, Ireland, by inductively coupled plasma atomic emission spectroscopy of lithium borate fusion glasses dissolved in nitric acid (ME-ICP06). This technique measured SiO<sub>2</sub>, Fe<sub>2</sub>O<sub>3</sub>, CaO, MgO, Na<sub>2</sub>O, K<sub>2</sub>O, Cr<sub>2</sub>O<sub>3</sub>, TiO<sub>2</sub>, MnO, P<sub>2</sub>O<sub>5</sub>, SrO and BaO. In addition, Nb and Zr were analysed by using Trace Level XRF Analysis (ME-XRF05) by ALS. Inductively coupled plasma mass spectroscopy analysis for trace elements was carried out at both the University of Brighton (UoB; Agilent 7900 ICP-MS) and the British Geological Survey (BGS, Keyworth; Agilent 7500 ICP-MS). Samples analysed at

BGS were prepared using a sodium peroxide fusion and those at UoB with a lithium metaborate fusion technique; in both cases fusion was followed by dissolution in concentrated nitric acid. Extended methodology for major and trace element analyses is provided in Supplementary Material S1. SINCLAS software was used to determine the normative mineralogy. Precision and accuracy were assessed by analysing the BHVO-2, W-2a, JB-1b, and SBC-1 Certified Reference Materials as unknowns at intervals during the analysis (Supplementary Material S1).

Petrographic analysis was carried out for 25 samples. Most petrographic samples have corresponding whole rock geochemical analyses, except for seven samples that were too heterogeneous or small for such analysis. Scanning electron microscope (SEM) imagery and analyses were done at BGS (Keyworth), using LEO 435VP variable pressure digital SEM and FEI Company Quanta 600 SEM instruments on carbon-coated (c. 25 μm) polished thin

sections, coated using an Emitech K950L high vacuum carbon evaporation coater. The LEO 435VP was operated in conventional high-pressure mode, accelerating voltages of 20 kV and 500 pA probe current; a four-quadrant solid-state detector was used to collect BSE imagery, and an Oxford Instruments INCA energy-dispersive X-ray microanalysis (EDXA) system was used to collect energy-dispersive X-ray (EDX) spectra for qualitative phase identification. The FEI Company Quanta 600 SEM was operated under high vacuum conditions ( $<1 \times 10^{-4}$  torr) and accelerating voltages of 10–20 kV; SEM photomicrographs were collected using backscattered electron (BSE) and cathodoluminescence (CL) techniques, the latter performed using a KE Developments Centaurus CL detector. An Oxford Instruments INCA Energy 450 EDXA system with a 50-mm<sup>2</sup> Peltier-cooled silicon drift detector X-ray detector was used to collect EDX spectra for qualitative phase identification.

Major element compositions of amphibole and pyroxene were determined on carbon-coated (30  $\mu\text{m}$ ) polished thin sections using a JEOL JXA-8200 electron microprobe (EMP) with wavelength dispersion spectrometry at Camborne School of Mines, University of Exeter, UK. Typical beam conditions used were a 15-kV accelerating voltage, 10-nA beam current, and 10- $\mu\text{m}$  beam diameter. These data were collected over three visits. Analytical conditions for the EMP are given in Supplementary Material S1.

Laser ablation inductively coupled plasma mass spectrometry (LA-ICP-MS) was used to collect a suite of trace element analyses for amphibole and pyroxene using a New Wave Research UP193FX excimer (193 nm) laser ablation system coupled to an Agilent 7500 series quadrupole ICP-MS at the British Geological Survey, Keyworth. The NIST SRM-610 glass was used as a standard and Si from EMP analyses used as the internal standard. Samples were presented as polished thin sections to LA-ICP-MS; an ablation time of 30 s at 5 Hz with a 50- $\mu\text{m}$  spot size was used to produce a  $\sim 15$ - $\mu\text{m}$  deep crater. Data reduction was done using Iolite v2.5 software (Paton et al., 2011). The NIST SRM-612 glass used for QA/QC and error was  $<5\%$  for the elements analysed.

## PETROGRAPHY

### Ampasibitika Ring Dyke

Syenites of the ARD are medium to coarse grained and exhibit orthocumulate textures. Often, there is a stark petrographic, and compositional, difference between the cumulate framework and subsequent interstitial assemblages. Commonalities between all syenites sampled include the following: alkali feldspar forms the main framework of the rock ( $>70$  vol %); amphibole- and clinopyroxene-group minerals are the major mafic phases, and these are either early magmatic or interstitial (Fig. 3a–e); discrete HFSE and REE minerals are more common in the later crystallising assemblages (Fig. 4a–d). We have subdivided syenites of the ARD into 5 units based on mineralogical evolution from calcic to sodic ferromagnesian assemblages (Fig. 3 and Table 1).

### Alkali feldspar syenites

*Type 1 alkali feldspar syenite (T1AfsSy; Fig. 3a)*: characterised by hypidiomorphic alkali feldspar ( $\sim 60$  vol %), rounded light green-yellow clinopyroxene (hedenbergite), olivine, and Fe–Ti-oxides. Alkali feldspar is generally medium to coarse grained (3 to 6 mm) and exhibits a hypidiomorphic granular texture, with perthite developed on some margins but cores lacking evidence for exsolution. Olivine is widely replaced by iddingsite, with fresh olivine only present as relics within these pseudomorphs. Fe–Ti-oxides exhibit trellis exsolution textures of ilmenite in magnetite.

Subhedral clinopyroxene crystals are strongly zoned, with dark green rims indicative of increasing aegirine content, especially when adjacent to interstitial assemblages. Dark green-brown amphibole and annite occur as interstitial crystals; amphibole forms overgrowths on partially resorbed clinopyroxene. Apatite lozenges ( $<1.5$  mm long) are located both within cumulate and interstitial assemblages; apatite in the interstitial assemblages has britholite overgrowths, which are variably replaced by REE-fluorcarbonates (e.g. bastnäsite, synchysite) (Fig. 4a). In some sections, comb-quartz lined, carbonate-filled miarolitic cavities (up to 5 mm wide) are present, interstitial to the alkali feldspar framework.

*Type 2 alkali feldspar syenite (T2AfsSy; Fig. 3b)*: medium- to coarse-grained alkali feldspar (0.5 to 3 mm) is the main cumulate phase; it is hypidiomorphic to tabular in texture and is often perthitic with rare unexsolved cores. Medium- to coarse-grained dark green clinopyroxene (aegirine) and dark green-brown amphibole occur within cores of schlieren structures; these are coarser grained than interstitial ferromagnesian phases in the surrounding syenite. These ferromagnesian schlieren are overgrown by dark blue-brown amphibole (arfvedsonite), rhythmically zoned dark to light green clinopyroxene and annite. Annite and dark blue-brown amphibole are the main interstitial mineral phases in the surrounding syenite. Within the T2AfsSy, miarolitic cavities up to 5 mm wide occur. These are lined with comb-textured quartz and filled with carbonate, fluorite, albite, annite, rhythmically zoned (light to dark green) clinopyroxene and microcrystalline quartz. In addition, a variety of HFSE-mineral phases are common. Carbonate is predominantly calcite, which is variably enriched in Fe and/or Mn. HFSE-mineral phases include skeletal pyrochlore group minerals, syntaxial intergrowths of REE-fluorcarbonates (bastnäsite, synchysite) and zircon. Clinopyroxene and amphibole in the alkali feldspar syenites are variably altered to carbonate minerals. Relic apatite is present within alteration assemblages, although in places it is pseudomorphed by REE-fluorcarbonates.

### Ankobabe Hybrids

The Ankobabe Hybrids encompass the nepheline syenites, here divided into three types, two recognised by Estrade et al. (2014a) plus an additional variant, and phonolite dykes and trachytic-phonolite enclaves.

*Type 1 nepheline syenite (T1NeSy; T-1 nepheline syenite of Estrade et al., 2014a; Fig. 3c)*: Tabular to moderately hypidiomorphic alkali feldspars (c. 3–5 mm) are variably interlocking and, alongside amphibole phenocrysts and agglomerates (c. 0.5–2 mm), form the main framework of this syenite. Ferromagnesian minerals include olivine, three varieties of clinopyroxene (partially resorbed hedenbergite, aegirine–augite coronae replacing amphibole and hedenbergite and interstitial aegirine) and amphibole (hastingsite cores (Am I), katophorite reaction rims (Am II) and arfvedsonite overgrowths (Am III)), annite and Fe–Ti-oxides (Estrade et al., 2014a). All clinopyroxene varieties are fine grained (0.5 mm). Alkali feldspar has coarse perthitic textures, with rare unexsolved cores, and nepheline is an interstitial phase. Both alkali feldspar and nepheline are variably replaced by analcime and natrolite. Apatite ( $<0.2$  mm) is a common accessory phase, occurring as inclusions within and on the margins of amphibole. Marginal apatite and that in contact with analcime has REE-rich overgrowths. Rare, very fine-grained monazite, Ca–Na-zirconosilicate and pyrochlore group minerals are present in the final interstitial space between analcime and aegirine (Fig. 4b).

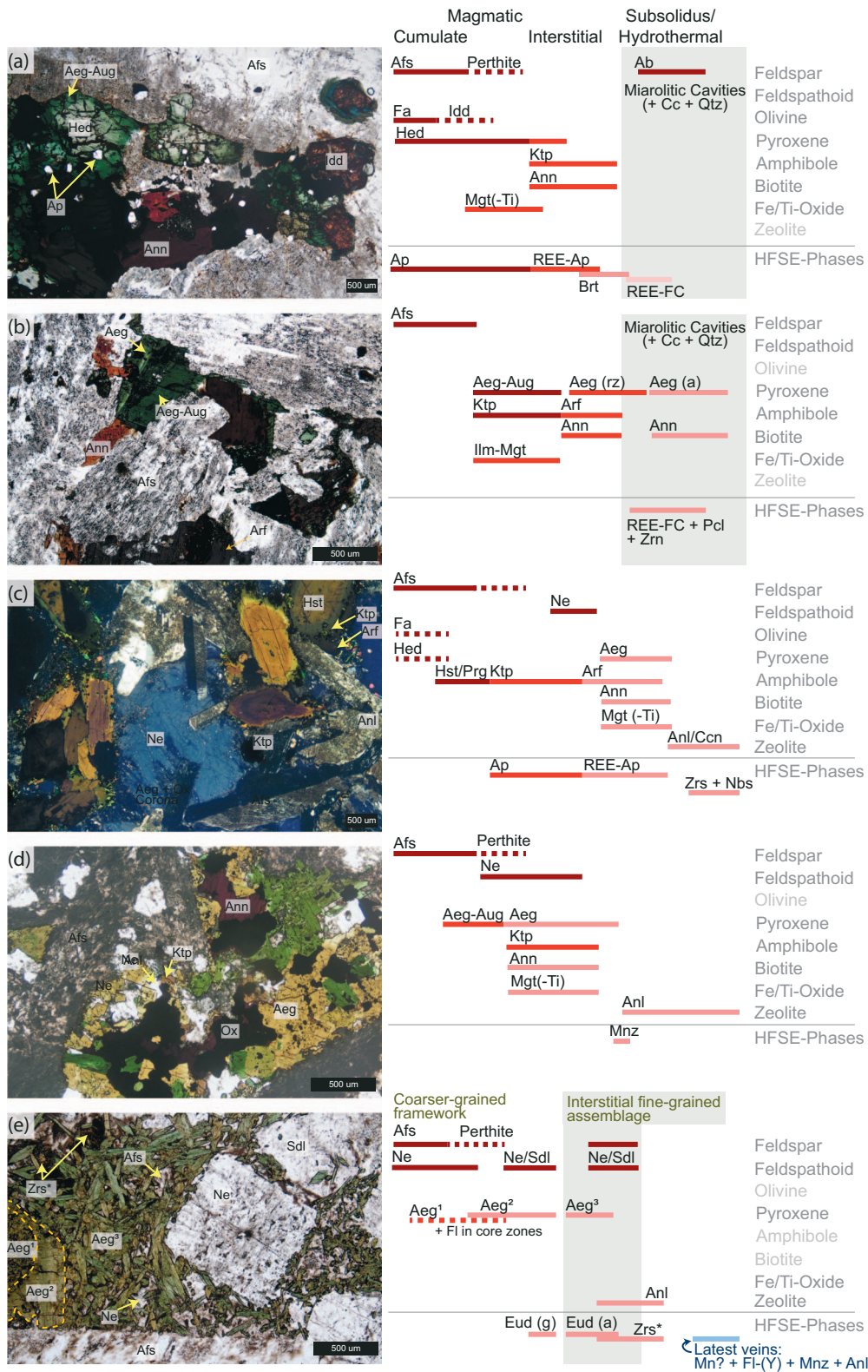


**Fig. 3.** Representative photomicrographs illustrating mineralogy and textures of Ampasibitika Intrusion syenites, accompanied by interpreted mineral paragenesis for: (a) T1AfsSy, (b) T2AfsSy, (c) T1NeSy, (d) T2NeSy and (e) T3NeSy. Mineral abbreviations: Ab; albite; Aeg, aegirine; Aeg-Aug, aegirine-augite; Afs, alkali feldspar; Anl, analcime; Ann, annite; Ap, apatite; Arf, arfvedsonite; Brt, britholite; Cc calcite; Ccn, cancrinite; Eud, EGMs; Fa, fayalite; Fl(-Y), yttrian-fluorite; Fl, fluorite; Hed, hedenbergite; Hst, hastingsite; Idd, iddingsite; Ilm-Mgt, ilmenite-magnetite exsolution; Ktp, katophorite; Mgt(-Ti), titanian-magnetite; Mn?, manganese-oxide/carbonate; Mnz, monazite; Nbs, niobosilicate; Ne, nepheline; Pcl, pyrochlore group minerals; Prg, pargasite; Qtz, quartz; REE-Ap, REE-rich apatite; REE-FC, REE-fluorocarbonate; Sdl, sodalite; Zrn, zircon; Zrs, zirconosilicate.

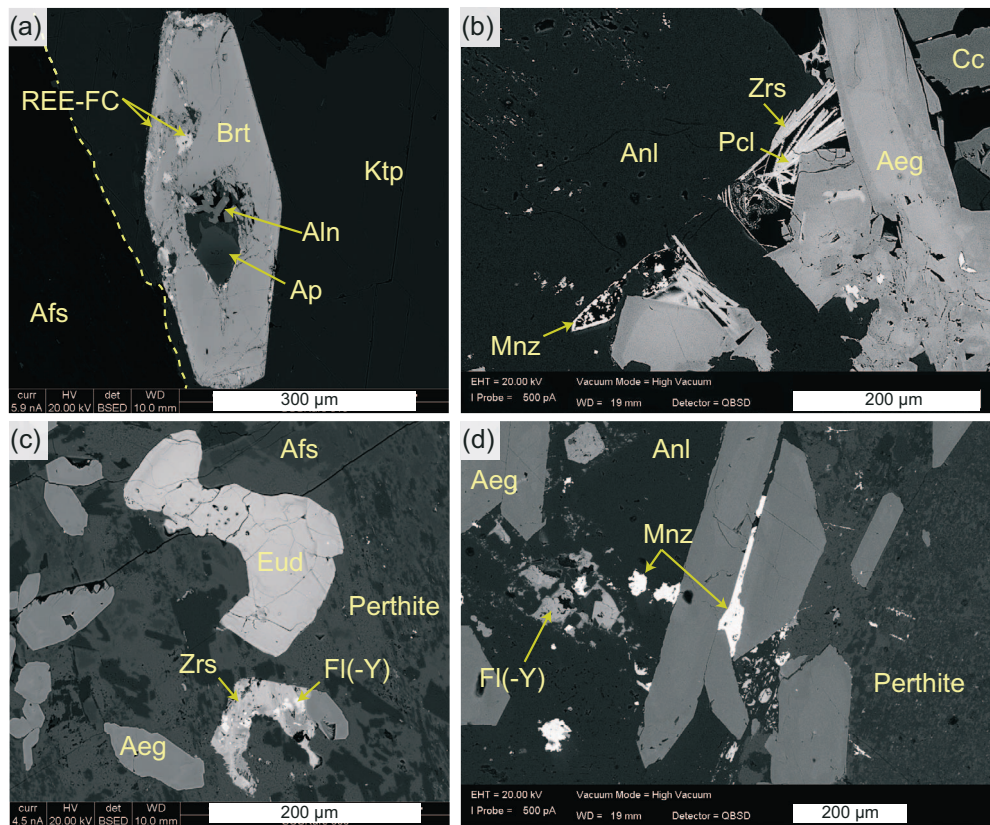


**Fig. 4.** (a) T1AfsSy partial replacement and overgrowth of apatite (Ap) by britholite (Brt), with associated allanite (Aln). Britholite is partially replaced by REE-fluorcarbonate, which comprises a symplectitic intergrowth of bastnäsite and synchysite. (b) T1NeSy, latest interstitial assemblage developed in void space between analcime and aegirine. Filaments of Ca-Na-zirconosilicate are interleaved with pyrochlore, monazite present as a coating on analcime. (c) T3NeSy, eudialyte and adjacent intergrown assemblage of Ca-Na-zirconosilicate plus REE-enriched (yttrian) fluorite inferred to represent pseudomorphic replacement of eudialyte (note: elsewhere these pseudomorphs also contain analcime, REE-fluorcarbonate and monazite). (d) Fracture cross-cutting T3NeSy, fine fractures (<0.5 mm wide) are filled with analcime, yttrian fluorite and monazite.

*Type 2 nepheline syenite (T2NeSy; T-II nepheline syenite— Estrade et al., 2014a ; Fig. 3d):* In this nepheline syenite type, olivine is absent. Estrade et al. (2014a) did not observe biotite; however, we observed annite alongside arfvedsonite, aegirine-augite, Fe-Ti-oxides and nepheline in equigranular, interstitial masses. Alkali feldspar laths (<4 mm) have a perthitic texture, and nepheline (<2 mm) is an interstitial phase.

*Type 3 nepheline syenite (T3NeSy; Fig. 3e):* A further type 3 nepheline syenite (T3NeSy) is recognised in this study. It is characterised by the presence of tabular perthitic alkali feldspar (<4 mm), euhedral nepheline (<2 mm), aegirine and fine-grained EGM (<0.3 mm; Fig. 4c) and absence of amphibole-group minerals. Aegirine occurs either as relatively large euhedral crystals, which may have granular core zones where finer-grained aegirine occurs with fluorite, or as acicular crystals forming a microcrystalline interstitial assemblage with nepheline, albite, and K-feldspar, and eudialyte. Eudialyte also occurs as globular masses interstitial to alkali feldspar laths (Fig. 4c) and as thin crystals associated within the microcrystalline assemblage. In places, eudialyte is replaced by masses of Ca-Na-zirconosilicate, fluorite and REE-fluorcarbonate and/or monazite, associated with analcime (Fig. 4c). Cross-cutting microcrystalline veins (<5 mm wide), visible in hand specimen, have the same mineralogy as the interstitial microcrystalline assemblage. Even later veins are dominated by analcime with minor fluorite-Y, monazite and a Mn-oxide/carbonate (Fig. 4d).

*Trachytic-phonolite enclaves:* The enclaves have a groundmass comprising fine-grained alkali feldspar, minor nepheline and aggregates of clinopyroxene, amphibole and Fe-Ti-oxides. Where associated with T1NeSy, xenocrysts of zoned hastingsite to katophorite with coronitic aegirine-augite overgrowths and alkali feldspar with inclusion-rich rims are abundant. Other enclaves, associated with the T2NeSy, have fewer xenocrysts but contain internal leucocratic blebs and ocelli. Ocelli are typically ~0.5 mm wide, but in places form clusters up to 3 mm in diameter. These ocelli contain nepheline and/or sodalite, variably replaced by analcime, and commonly contain singular euhedral titanite crystals (<0.2 mm). Amoeboid leucocratic blebs comprise variable proportions of alkali feldspar, nepheline and sodalite, and contain disseminated fluorite (<0.01 mm). Imagery of ocelli and leucocratic plebs are provided in Supplementary Material S1 for reference. Agglomerations of fine-grained amphibole and biotite form zoned, spherical clusters, which locally contain Ti-magnetite, apatite and minor sulphides. Rare skeletal diopside phenocrysts (up to 1 mm) are variably replaced by amphibole.

*Phonolite dykes:* Phonolite dykes occur associated with both the northern and southern occurrences of nepheline-bearing syenites. Although all contain nepheline and other foidolitic phases, there are distinct mineralogical and textural differences. In the southern occurrence, the phonolite is fine to medium grained, composed of brown amphibole laths (<0.2 mm), which have corona overgrowths of green aegirine and Fe-Ti-oxides (reminiscent of textural relationships in the T1NeSy), in a

**Table 1:** Summary of major intrusive rocks identified within the Ampasibitika Ring Dyke and Marginal Dyke Swarm

Lithodeme	Unit		Occurrence	Characteristics	
Ampasibitika Ring Dyke (ARD)	Alkali feldspar syenites	Type 1 alkali feldspar syenite (T1AfsSy)	Sampled in core (TAND097) intersecting outer NE margin of ring dyke.	Coarse to very coarse grained. Hypidomorphic Afs (~80%). Px as inclusions and equigranular, Px > Am.	
		Type 2 alkali feldspar syenite (T2AfsSy)		Vari-textured. Medium to pegmatitic. Hypidomorphic Afs (~80%). Px + Am interstitial, Px ≈ Am.	
	Ankobabe hybrids	Nepheline syenites	Type 1 nepheline syenite (T1NeSy)	Inner margin of ring dyke. Present in outcrops and as boulders close to apex of annular ridge.	Medium to coarse grained. Tabular Afs network (~80%), Am equigranular/phenocryst, Am > > Px. Ne interstitial.
			Type 2 nepheline syenite (T1NeSy)		Medium to coarse grained. Tabular Afs network (~70%), Am + Px equigranular, Am ≈ Px. Ne interstitial.
		Type 3 nepheline syenite (T3NeSy)		Medium-grained + fine-grained interstitial assemblage, tabular Afs network (~60%), Px in phenocrysts, granular cores and acicular forms. Ne as euhedral phenocrysts and interstitial.	
		Trachytic-phonolite enclaves		Varied: Fine-grained, comprised of Afs, Ne, Cpx, Am and Fe-Ti Ox phases, with a variety of xenocrysts, leucocratic blebs and ocelli.	
Marginal Dyke Swarm (MDS)		Phonolite dykes	Cross-cutting nepheline syenite outcrops within inner margin of the ARD.	Varied: fine grained of variable mineralogy, although all containing Ne and other foidolitic phases.	
		Peralkaline granite dykes	Dykes located on outer flanks of the ARD. Intruded bedded sedimentary units of the Isalo Group. Present as both individual and mixed (granite + quartz-microsyenite/trachyte) intrusive units.	GR-I: equigranular, medium to coarse grained. GR-II and GR-III: aplitic to pegmatitic, with well-developed layering.	
		Microsyenite dykes		Fine to medium grained, equigranular to porphyritic trachytic texture. Phenocrysts, when present, are dominantly alkali feldspar. Often altered (sericitised).	

groundmass of nepheline and alkali feldspar microlites that are extensively altered to sericite and possible cancrinite. In contrast, phonolite in the northern area is fine to very fine grained, and has a porphyritic microlitic texture with a groundmass of aegirine microlites (<0.2 mm) in a mosaic of alkali feldspar, nepheline and sodalite. Leucocratic lenses of medium-grained sodalite, nepheline and alkali feldspar are aligned sub-parallel to the dyke margin, and alkali feldspar phenocrysts are variably resorbed. Thin fluorite veins cross-cut the dyke; pyrochlore group minerals, monazite, apatite and titanite are present within these veins and the surrounding alteration halos.

## Marginal Dyke Swarm

**Microsyenite Dykes:** In general, quartz-microsyenites are characterised by tabular sericitised alkali feldspar phenocrysts embedded in a matrix of alkali feldspar and quartz microlites, with

interstitial carbonate (calcite and siderite) and Fe-oxides. Locally, fine-grained REE-fluorocarbonates and zircon are associated with Fe-oxides.

PGDs: Our observations are consistent with [Estrade et al. \(2018, 2015\)](#). These studies describe the textural and mineralogical features of the PGDs in detail. In general, these different granites are characterised by the following features:

GR-I, homogeneous medium- to coarse-grained miaskitic granite consisting of alkali feldspar, quartz and arfvedsonite or aegirine or both.

GR-II, commonly pegmatitic granite with banded texture resulting from variations in colour, grain size and modal mineralogy. In aplitic layers, dark green bands have greater proportion of aegirine and lighter bands have higher alkali feldspar content. In pegmatitic layers, coarse-grained quartz, alkali feldspar and sodic-amphibole exhibit unidirectional

growth textures perpendicular to dyke margins. The GR-II is transitional between apgaitic and miaskitic with the development of secondary pseudomorph assemblages after precursor HFSE minerals, such as EGM (Estrade *et al.*, 2014b). GR-II observed in this study was coarse grained with a pegmatitic texture, comprising euhedral blue sodic amphibole, fluid- and mineral-inclusion rich quartz, alkali feldspar, orange-brown pyrochlore group minerals and euhedral to subhedral accumulations of dendritic to botryoidal zircon and quartz. The latter are consistent with type 1 pseudomorphs after EGM described by Estrade *et al.* (2014b).

Generally, the GR-III, mesocratic to melanocratic, banded, apgaitic granitic pegmatite is rich in EGM, aegirine and sodic-amphibole (Estrade *et al.*, 2014b, 2018). The GR-III of this study has a banded aplitic texture produced by varying grain size and quartz abundance. Bright green aegirine and blue sodic-amphibole, quartz, alkali feldspar, fluorite and various fine-grained HFSE phases (e.g. REE-fluorocarbonate, fergusonite) comprise GR-III. Carbonate is a ubiquitous phase, developing as halos surrounding clinopyroxene or filling interstitial space. Fluorite veins, originating from the GR-III core, cross-cut aplitic bands and intrude surrounding country rock. Quartz is variably inclusion rich; in coarser grained quartz lenses (quartz >2 mm) inclusions are restricted to cross-cutting trails, whereas quartz that is finer grained, but not aplitic, contains abundant inclusions. Detailed investigation of the inclusions is beyond the scope of this study, but it is apparent these inclusions include mineral (fluorite, aegirine, blue amphibole) and melt/vapour varieties. Although lacking apgaitic mineral phases, the abundance of HFSE phases and textural and mineralogical characteristics indicate this dyke is more like the GR-III described by Estrade *et al.* (2014b) than GR-II.

## MINERAL CHEMISTRY

### Amphibole major element chemistry

Formula calculations for amphibole analyses were performed using the Excel spreadsheet of Locock (2014), based on 24 (O, OH, F, Cl), and were classified using IMA 2012 recommendations (Hawthorne *et al.*, 2012; Oberti *et al.*, 2012). The amphiboles analysed belong to the calcic-, through sodic-calcic, to sodic-subgroups.

Interstitial amphibole of the T1AfsSy is classified as ferro-ferri-katophorite. In the T2AfsSy amphibole occurs in schlieren cores and as interstitial crystals. Schlieren cores have compositions between ferro-ferri-katophorite and ferro-richterite, whereas schlieren rim and interstitial amphibole range from ferro-ferri-katophorite to arfvedsonite. Katophoritic amphibole of the T1AfsSy and T2AfsSy can further be divided into Ca-rich and Ca-poor varieties, with marginal (later crystallised) katophorite exhibiting lower Ca content (<1 apfu). This reduction in Ca is not associated with an increase in Si (Fig. 5a) or decrease in Al.

As described by Estrade *et al.* (2014a), partially resorbed core amphibole in the T1NeSy is classified as hastingsite (Am I), and the subsequent overgrowths are of ferro-ferri-katophorite (Am II) proximal to the cores become progressively Na-enriched, with arfvedsonite forming the outermost overgrowths (Am III; Fig. 7a). Interstitial amphibole of the T2NeSy ranges from arfvedsonite to ferro-ferri-nybøite. Amphibole in one such sample of T2NeSy from the Ankobabe Boulder Field exhibits elevated Mg and Mn, up to 0.5 and 0.4 apfu, respectively, relative to arfvedsonite of the T1NeSy; this nepheline syenite sample contains trachytic-phonolite enclaves; therefore, the elevated concentrations may reflect interaction of these phases during amphibole crystallisation.

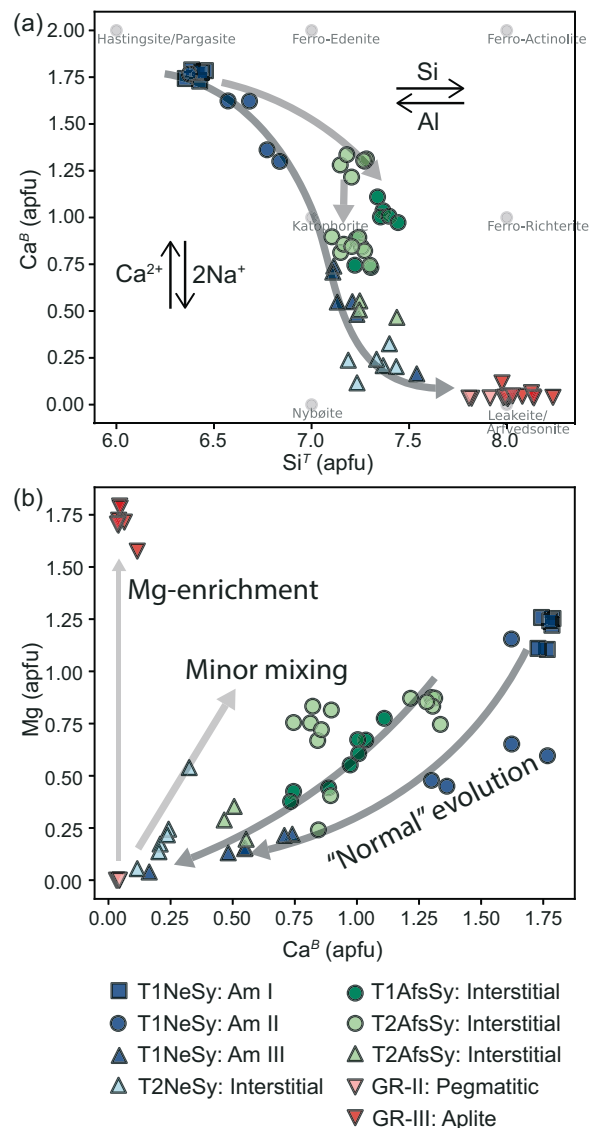


**Fig. 5.** Trends in cation proportions in amphibole: (a) Si vs Ca (B-site), with Hawthorne *et al.* (2012) end-member amphibole compositions for reference and (b) Ca (B-site) vs Mg.

Consistent with the results of Estrade *et al.* (2018), fine-grained amphibole of GR-III is ferri-fluoro-leakeite and pegmatitic amphibole of GR-II is fluoro-arfvedsonite. Magnesium is relatively enriched in GR-III ferri-fluoro-leakeite (Mg 1.6–1.7 apfu) relative to GR-II fluoro-arfvedsonite (Mg b.d.l.). Similar Mg enrichment is observed in GR-III clinopyroxenes (see Clinopyroxene major element chemistry).

Fluorine is elevated relative to chlorine in all amphibole analyses and is highest in fluoro-arfvedsonite of the GR-III PGD. Fluorine typically increases with decreasing Al in the nepheline syenites and T1AfsSy; however, in the T1NeSy, the latest, most sodic, katophorite to arfvedsonite rims are slightly depleted in F relative to the intermediate, relatively Ca-rich, katophorite.

### Clinopyroxene major element chemistry

Clinopyroxene is a major to minor mafic phase in samples of the ARD syenites and some PGD of the dyke swarm (MDS). Structural formulae of clinopyroxene were calculated based on four cations

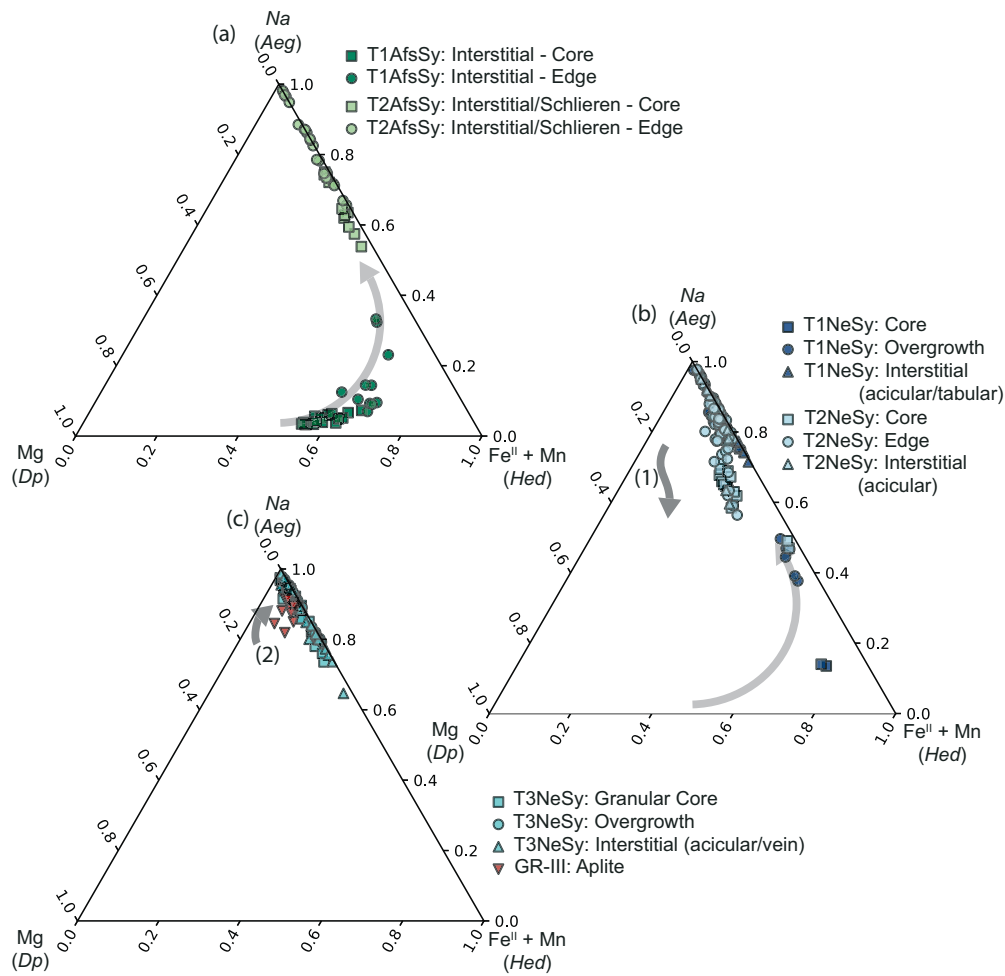


**Fig. 6.** Major element compositional trends for clinopyroxenes of intrusive units of the Ampasibitika Intrusion in Na (Aeg, Aegirine)–Fe(II) + Mn (Hed, Hedenbergite)–Mg (Dp, Diopside) ternary space: (a) T1AfsSy and T2AfsSy, (b) T1NeSy and T2NeSy, and (c) T3NeSy and G-III. In general, clinopyroxenes transition to increasingly aegirine-rich compositions. Deviation from this includes trend (1) shift in clinopyroxene compositions to more diopsidic (Mg) character in some T2NeSy analyses, these are located in T2NeSy that are adjacent to mingled trachytic-phonolite enclaves; and trend (2), some GR-III aegirine compositions exhibit more diopsidic compositions, these are restricted to core zones of clinopyroxenes analysed.

and six oxygens, and the 10 endmember compositions of clinopyroxene were calculated using the method of Marks *et al.* (2008). These are given in Supplementary Material S2. Major components of clinopyroxenes analysed are hedenbergite and aegirine. Magnesium content is ubiquitously low, with a maximum average  $X_{Mg}$  ( $Mg/[Mg + Fe^T]$ ) of 0.39 attained in hedenbergite cores of the T1AfsSy. Figs 6a–c show clinopyroxene analyses projected in the aegirine–diopside–hedenbergite (Na–Mg–Fe + Mn) ternary space.

Clinopyroxene of the T1AfsSy shows a gradual change in composition from hedenbergite in the light green cores to aegirine–augite in the dark green rims. Clinopyroxene in the T2AfsSy varies from aegirine–augite to near endmember aegirine compositions, with the former forming homogeneous dark green cores and the latter rhythmically zoned overgrowths in both schlieren and interstitial assemblages.

The T1NeSy contains three varieties of clinopyroxene: partially resorbed hedenbergite cores, aegirine–augite to aegirine coronae, and interstitial acicular to tabular aegirine crystals. Diopsidic clinopyroxene reported by Estrade *et al.* (2014a) in the T1NeSy is similar in major element composition to the T1AfsSy of this study. Analyses of core clinopyroxene in the T1NeSy were of aegirine–augite composition; these cores are extensively resorbed, and thus may not represent primitive clinopyroxene composition.

Element mapping of a characteristic T1NeSy assemblage highlights the observation of Estrade *et al.* (2014a) that clinopyroxene crystals occurring with Fe–Ti-oxide in coronae after katophorite are relatively Ca richer, whereas prismatic clinopyroxene crystals associated with analcime are Ca poorer (Fig. 7a). In the T2NeSy, clinopyroxene compositions range from aegirine–augite to near endmember aegirine. Some analyses from mingled T2NeSy samples, containing both nepheline syenite and an adjacent trachytic-phonolite enclave, have elevated Mg content with displacement towards diopsidic compositions (Fig. 6b, trend 1).

The T3NeSy contains clinopyroxene as euhedral crystals, some with granular core zones, or as acicular crystals in the microcrystalline interstitial assemblage. All these clinopyroxene types are aegirine dominant (>70 mol % Aeg; Fig. 6c). Compositional differences between clinopyroxene varieties include high Al content of aegirine overgrowths (avg. 1.6 wt %  $Al_2O_3$ ) relative to acicular (avg. 1.2 wt %  $Al_2O_3$ ) and granular (avg. 0.9 wt %  $Al_2O_3$ ) aegirines; elevated Mn and depleted Ti in granular aegirine (avg. 0.52 wt % MnO; 0.16  $TiO_2$ ) relative to other aegirine types (avg. 0.29–0.34 wt % MnO; 0.44–0.48 wt %  $TiO_2$ ). Element mapping of the different aegirine varieties indicates finer oscillations in composition, with enrichments in Ca and, more subtly, Mn developed on rims of acicular and overgrowth aegirine varieties (Fig. 7b).

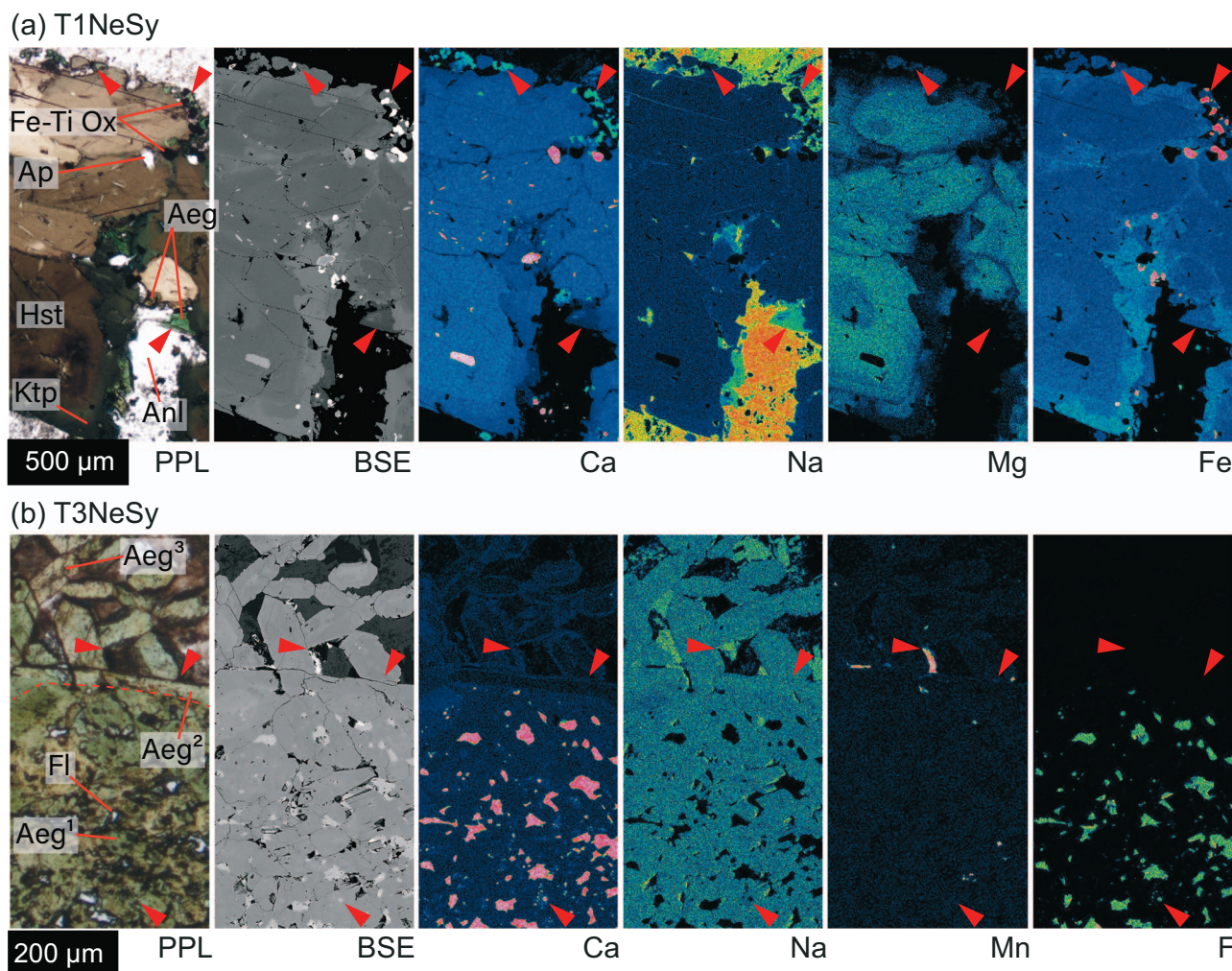


**Fig. 7.** Element maps showing fine-scale variation in amphibole and pyroxene compositions, with red arrows pointing to representative locations of subtle chemical variation, within (a) T1NeSy showing variation in Ca, Na, Mg and Fe in a typical zoned amphibole (hastingsite to katophorite to arfvedsonite overgrowths) with both aegirine coronae and interstitial acicular aegirine; and (b) T3NeSy showing variation in Ca, Na, Mn and F, highlighting small-scale variations in aegirine compositions and presence of fluorite in granular core zones, as well as presence of Mn phases as late crystallisation products on margins of acicular aegirine.

Although all aegirine rich (77–84 mol % Aeg), some GR-III aegirine analyses show enrichment towards diopsidic compositions (Fig. 6c, trend 2), containing up to 1.5 wt % MgO. This trend is coupled with increased Ca (max. 7.3 wt % CaO) and Mn (max. 0.62 wt % MnO) in these aegirines. Detailed analysis by Estrade *et al.* (2019) of similar GR-III aegirine shows this elevated Mg, Mn and Ca signature is restricted to core zones.

## AMPHIBOLE AND CLINOPYROXENE TRACE ELEMENT COMPOSITIONS

Trace element analyses are grouped by rock type (Fig. 8a–e), and where applicable, variations in trace element characteristics are described relative to mineral varieties. The fine-scale oscillations in clinopyroxene chemistry, indicated by element maps, are below the resolution of LA-ICP-MS spot analyses.

### Amphibole

The majority of amphiboles in syenites of the ARD have similar trace element profiles. Commonalities in chondrite-normalised trace element profiles include negative Ba, Rb, K, Sr and Eu anomalies, and typically positive Nb and Zr anomalies (Fig. 8 a,

c). Light REE (LREE) and HREE are enriched relative to middle REE (MREE) in amphiboles and exhibit negative Eu anomalies ( $\text{Eu}/\text{Eu}^*$ : 0.02–0.28). However, absolute REE concentrations and the proportion of LREE to HREE vary considerably, with decreasing  $\text{La}/\text{Yb}_{\text{cn}}$  and  $\Sigma\text{REE}$  as amphiboles become increasingly sodic. Niobium and Zr are variable but generally exhibit strong positive anomalies.

The  $\text{La}/\text{Yb}_{\text{cn}}$  ratio and  $\Sigma\text{REE}$  are greatest in hastingsite of the T1NeSy (avg. 13.4  $\text{La}/\text{Yb}_{\text{cn}}$ ; 1283 ppm  $\Sigma\text{REE}$ ) and decrease with increasing  $\text{Na}_2\text{O}$ . This relative enrichment of HREE ( $<\text{La}/\text{Yb}_{\text{cn}}$ ) in increasingly sodic amphiboles is a common feature of amphiboles of alkaline to peralkaline complexes (Marks *et al.*, 2004; Siegel *et al.*, 2017).

Lithium becomes increasingly enriched as amphiboles become more sodic; the lowest Li concentrations are recorded in katophorite and hastingsite of the T1AfsSy (avg. 77.6 ppm Li) and T1NeSy (avg. 53.6 ppm Li), and highest in ferro-ferri-fluoro-leakeite in the GR-II PGD (avg. 3004 ppm Li).

### Pyroxene

The majority of clinopyroxene crystals in syenites of the ARD have similar chondrite-normalised trace element profiles. Commonalities include negative Ba, Pb, Sr and Eu anomalies (Fig. 8d–e).

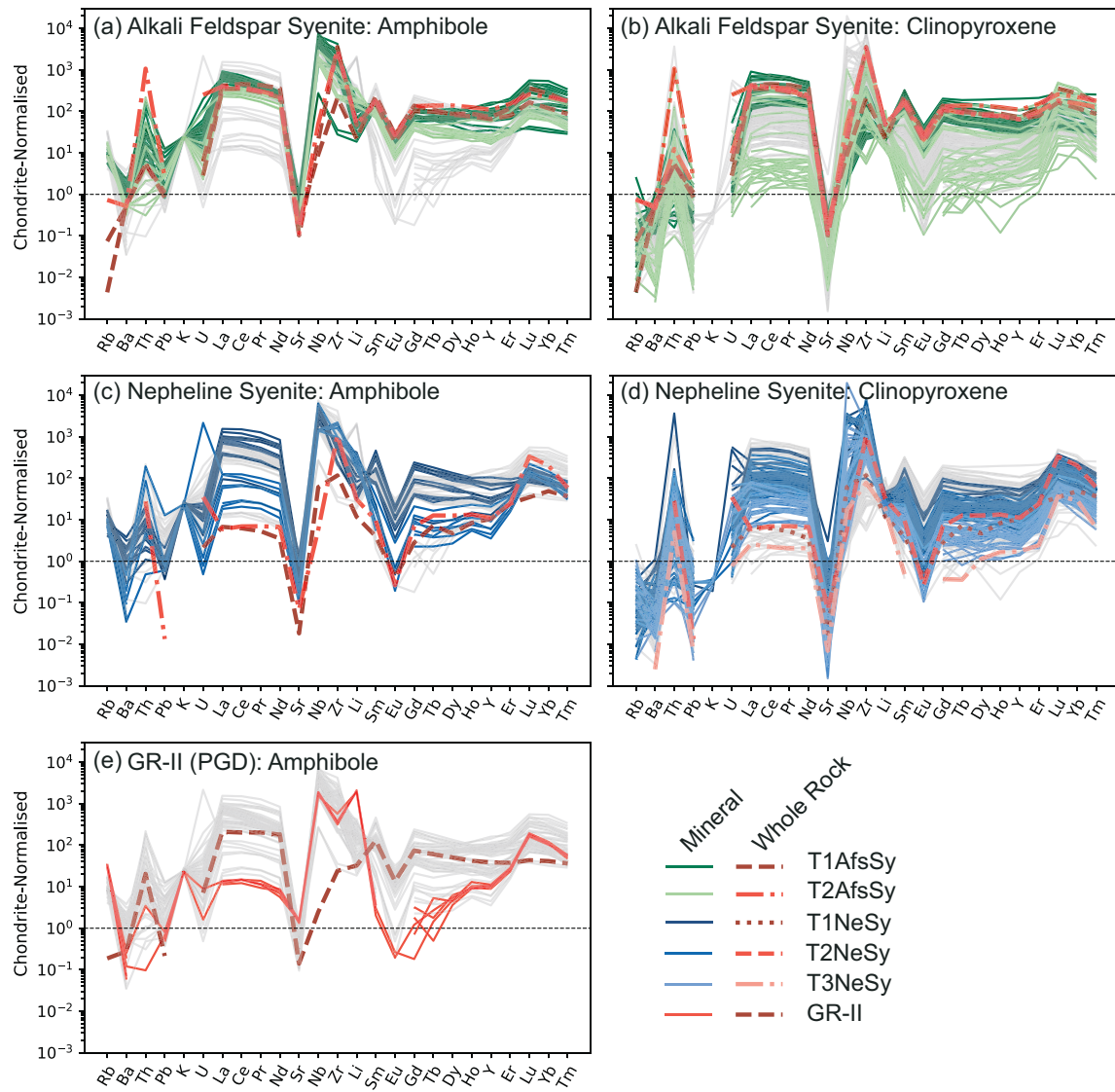


**Fig. 8.** Chondrite-normalised trace element profiles for amphibole- (left column) and clinopyroxene-group (right column) minerals of the Ampasibitka Intrusion, displayed alongside whole rock compositions of samples analysed for (a, b) T1AfsSy and T2AfsSy, (c) T1NeSy and T2NeSy, (d) T1NeSy, T2NeSy, and T3NeSy, and (e) GR-II. Light grey lines represent all analyses of amphibole- (a, c, e) and clinopyroxene-group (b, d) minerals.

Zirconium exhibits negative to neutral anomalies in hedenbergite, whereas more sodic pyroxenes (aegirine) generally exhibit strong positive Zr anomalies. As in the amphibole, REE patterns have concave upwards profiles, with LREE and HREE enriched relative to MREE, with negative Eu anomalies ( $\text{Eu}/\text{Eu}^*$ : 0.00–0.33). In general, clinopyroxenes of the ARD syenites exhibit a continuous evolution from LREE-enriched chondrite-normalised REE patterns in the early calcic varieties (diopside to hedenbergite), through sinusoidal patterns for intermediate Ca–Na varieties (aegirine–augite) to strongly HREE-enriched, in late sodic varieties (aegirine).

Lithium exhibits variable behaviour and is most enriched in zoned aegirine of the T2AfsSy (17.2 to 155 ppm Li). Zirconium and Ti are enriched in variable proportions in clinopyroxene both within and between in ARD syenite varieties, with concentrations ranging from below detection limit to percentage levels (up to 3.25% Zr and 1.15% Ti). Relative to Zr and Ti, Nb is present in lower abundances in clinopyroxenes and is most enriched in aegirine of the nepheline syenite and alkali feldspar syenites.

For both amphibole and pyroxene, total REE concentrations typically decrease as these phases become increasingly sodic.

The LREE typically show greater degrees of depletion than HREE. HREE exhibit more variable behaviour, with HREE enriched in sodic relative to calcic counterparts in the T1AfsSy and depleted (albeit to a lesser extent than LREE) in clinopyroxenes of the T1NeSy, T2NeSy and T2AfsSy. Amphiboles exhibit more consistent behaviour, with HREE (predominantly Lu, Yb, Tm) enriched in sodic varieties relative to calcic counterparts.

## BULK ROCK GEOCHEMISTRY

Bulk rock compositions are summarised in Table 2 and presented in full in Supplementary Material S2. Additional data for the ARD from (Estrade *et al.*, 2014a; Estrade *et al.*, 2014b) are included for comparison. Compositionally, rocks of the ARD are remarkably diverse, ranging from metaluminous and peraluminous to peralkaline (Fig. 9a), and silica-oversaturated, silica-neutral and silica-undersaturated (Fig. 9b), and exhibiting a wide range of total REE concentrations.

All rocks of the ARD are relatively  $\text{SiO}_2$  rich ranging from 55.9 in the phonolite dykes to 73% in the GR-III (Fig. 9c, d). The highest

**Table 2:** Summary of compositional signatures of Ampasibitika Intrusion units

Lithodeme	Unit	Silica saturation [FSSI]	Alkalinity [A/CNK; A/NK]	QAPF	
ARD	<b>Alkali feldspar syenites</b>	Neutral [−0.02 to 0.00]	Metaluminous/peralkaline [0.79 to 0.96; 0.96 to 1.04]	(Foid-bearing) alkali feldspar syenite	
	<b>Nepheline syenites</b>	Undersaturated [−0.10 to −0.49]	Metaluminous to peralkaline [0.78 to 0.99; 0.83 to 1.14]	Foid-bearing alkali feldspar syenite to Foid Syenite	
	<b>Ankobabe hybrids</b>	<b>Trachytic-phonolite enclaves</b>	Undersaturated [−0.13 to −0.32]	Metaluminous to peralkaline [0.77 to 0.93; 0.95 to 1.07]	Foid-bearing alkali feldspar syenite to Foid Syenite
	<b>Phonolite dykes</b>	Undersaturated [−0.25 to −0.53]	Peralkaline (to peraluminous) [0.77 to 1.06; 0.83 to 1.22]	Foid Syenite	
MDS	<b>Microsyenite dykes</b>	Neutral to oversaturated [0.00 to 0.26]	Metaluminous, peraluminous and peralkaline [0.66 to 1.11; 0.98 to 1.59]	Alkali feldspar syenite to Syeno-Granite	
	<b>PGD</b>	Oversaturated [0.08 to 0.36]	Peralkaline [0.28 to 0.97; 0.39 to 1.12]	Alkali Feldspar Granite	

Al<sub>2</sub>O<sub>3</sub> contents also vary considerably, from 6.38 wt % in the GR-III to 21.4 wt % in the phonolite dykes (Fig. 9c). Alkali contents are high (>5.13 Na<sub>2</sub>O+K<sub>2</sub>O), reaching a maximum of 16 wt % Na<sub>2</sub>O+K<sub>2</sub>O in the T3NeSy of the Ankobabe Hybrids (Fig. 9d). Alkali concentrations are lower in MDS units, likely reflecting the abundance of quartz (> SiO<sub>2</sub>) relative to alkali-rich phases (e.g. alkali feldspar) or variable albitisation of the Microsyenite and PGDs. The ARD units show increasingly sodic compositions, whereas the MDS units do not exhibit a clear evolutionary trend in alkali contents (Fig. 9d, e).

Nepheline and alkali feldspar syenites of the ARD all have relatively low MgO (<0.6 wt %), TiO<sub>2</sub> (<0.8 wt %), CaO (<2.13 wt %), MnO (<0.23 wt %) and P<sub>2</sub>O<sub>5</sub> (<0.15 wt %). Phonolite dykes and trachytic-phonolite enclaves have similar compositions to the nepheline syenites, although some have slightly elevated MgO (max. 1.08 wt %), CaO (max. 2.96 wt %) and TiO<sub>2</sub> (max. 0.98 wt %) contents. Dykes of the MDS also have low MgO (<0.56 wt %), MnO (<0.59 wt %) and TiO<sub>2</sub> (<0.49 wt %), and low to moderately high CaO (0.35–6.16 wt %). Fe<sub>2</sub>O<sub>3</sub> typically ranges from 4.48 to 6.24 wt % in the ARD alkali feldspar syenites and all components of the Ankobabe Hybrids (there is a higher value of 9.21 for one of the T2AfsSy samples, but this sample is visibly altered). In the MDS, Fe<sub>2</sub>O<sub>3</sub> generally ranges from 5.82 to 7.93 wt %, with the exception of the GR-I dykes that, as reported by Estrade et al. (2014a, 2014b), have elevated Fe content.

REE and Zr concentrations vary considerably, typically showing an increase in concentration from alkali feldspar syenites, through nepheline syenite and microsyenite dykes, to the highest values in the PGD. Total REE concentrations range from 110 ppm (T1AfsSy) to 16 734 ppm (GR-III); Zr shows a similar variation from 102 ppm (T1AfsSy) to 13 364 ppm (GR-III).

Divergence of SiO<sub>2</sub> contents of the silica-neutral to silica-undersaturated ARD syenites and the silica-oversaturated MDS mean that the term ‘evolved’ reflects decreasing SiO<sub>2</sub> content in the former (SiO<sub>2</sub> 62–54.6 wt %) and increasing SiO<sub>2</sub> content in the latter (SiO<sub>2</sub> 58.8–76.8 wt %; Fig. 10a). Due to this divergence of SiO<sub>2</sub> and Al<sub>2</sub>O<sub>3</sub> trends and the variability of SiO<sub>2</sub>, K/Rb is used as a proxy of melt evolution (Fig. 10a–f).

Fe<sub>2</sub>O<sub>3</sub> does not show significant variation with K/Rb (Fig. 10b), with the exception of the PGD dykes of the dyke swarm (MDS), which exhibit elevated Fe from K/Rb ~100 and subsequently

display a weak negative trend as K/Rb further decreases (Estrade et al., 2014a, 2014b). Na<sub>2</sub>O increases with decreasing K/Rb in the ARD; however, there is no clear trend in the MDS (Fig. 10c). MnO also does not show significant variation with K/Rb, with the exception of the GR-III dykes that exhibit a pronounced increase in MnO (Estrade et al., 2014a, 2014b) (Fig. 10d). Generally, Zr and REE increase with decreasing K/Rb. Notably, some nepheline syenites that contain sodic clinopyroxenes and amphiboles fall below Zr and REE concentrations expected for the degree of melt evolution indicated by K/Rb (Fig. 10e, f).

We have chosen to normalise trace element data to average Ocean Island Basalt (OIB) (Sun & McDonough, 1989) because mafic dykes cross-cutting the Ampasibitika Intrusion have trace element signatures comparable to OIB (Estrade et al., 2014a) (Fig. 11). Most units of the Ampasibitika Intrusion are depleted in Ba, Sr, P, Eu and Ti, indicative of feldspar, Fe–Ti-oxide and apatite fractionation. Trachytic-phonolite enclaves exhibit the least fractionated OIB-normalised trace element profiles, with minor depletions in Sr, P and Ti. In all units of the Ampasibitika Intrusion, the LREE are consistently enriched relative to the HREE. Relative to chondrite, La is enriched by a factor of 110 to 16 189, whereas La and Yb have enrichment factors of 6.9 to 1683, respectively. Relative enrichment of HREE to LREE varies from 4.3 ≤ [La/Yb]<sub>cn</sub> ≤ 68, with a mean [La/Yb]<sub>cn</sub> of 14.1 ± 8.6σ.

## DISCUSSION

The Ampasibitika Intrusion is a rare example of an alkaline-peralkaline sub-volcanic system with REE-enrichment in peralkaline silica-oversaturated lithologies. The results described above enable us to provide further constraints on the origin and evolution of the Ampasibitika Intrusion and the associated REE mineralisation.

### Ampasibitika Ring Dyke heterogeneity

Structurally, the Ampasibitika Intrusion exhibits features of a classic caldera with a circumferential dyke swarm (MDS) surrounding a ring dyke (ARD) that bounds a central caldera depression filled with volcanic and volcanoclastic material (Central Caldera Volcanics; Fig. 1).

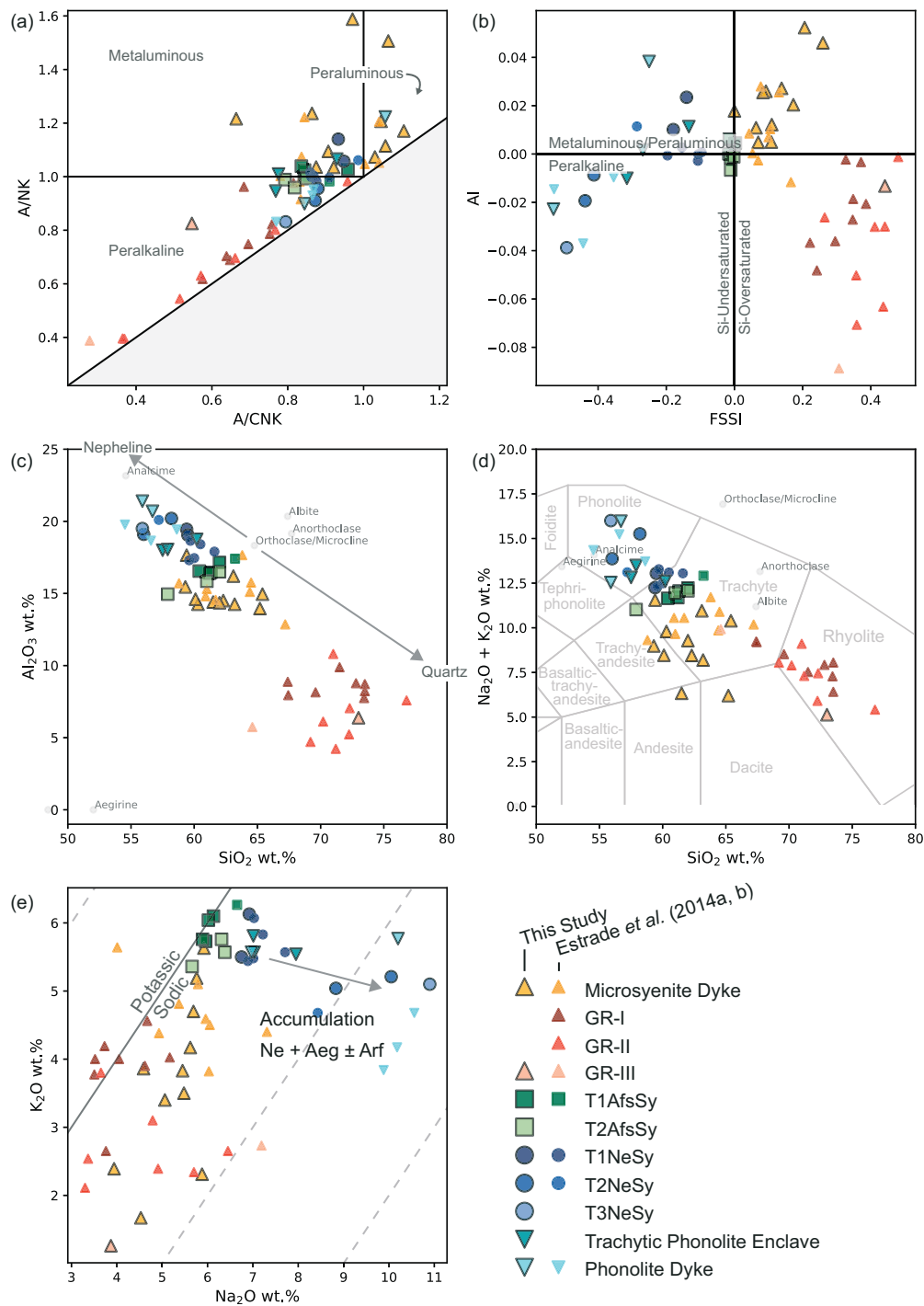


**Fig. 9.** Bivariate plots of the Ampasibitika Intrusion showing (a) A/CNK (molar ratio of  $Al_2O_3/CaO + Na_2O + K_2O$ ) vs A/NK (molar ratio of  $Al_2O_3/Na_2O + K_2O$ ), (b) alkalinity index (AI =  $Al - (K + Na)$ ) on a molecular basis vs feldspathoid silica saturation index (FSSI = normative  $Q - [Lc + 2(Ne + Kp)]/100$ ) discrimination plot of Frost & Frost (2008), (c)  $SiO_2$  vs  $Al_2O_3$ , (d) total alkali silica plot ( $SiO_2$  vs  $Na_2O + K_2O$ ) and (e)  $Na_2O$  vs  $K_2O$ .

Field relationships within the ARD, such as development of enclaves and dykes in the Ankobabe Hybrids, indicate the introduction of multiple, compositionally contrasting, magma batches (Fig. 2a–c). Angular to lobate dyke and enclave geometries are consistent with differing degrees of crystallinity of the syenitic crystal mushes and phonolitic to trachytic-phonolite melts (Barbarin & Didier, 1992; Barbarin, 2005). Xenocrysts derived from the syenites within the phonolite dykes and trachytic-phonolite enclaves indicate these

syenites were partially crystallised at the time of magma mingling.

Textural and chemical variation within ring fault intrusions (ring dykes) may arise during syn-caldera collapse, when mushy melts are displaced by subsidence of a central block (or blocks) and trapped within the ring fault(s) (Kennedy & Stix, 2007; Kennedy et al., 2018). Vortices formed during subsidence (Kennedy et al., 2018) may promote assembly of a range of materials within ring dykes, displaced from stratified layers

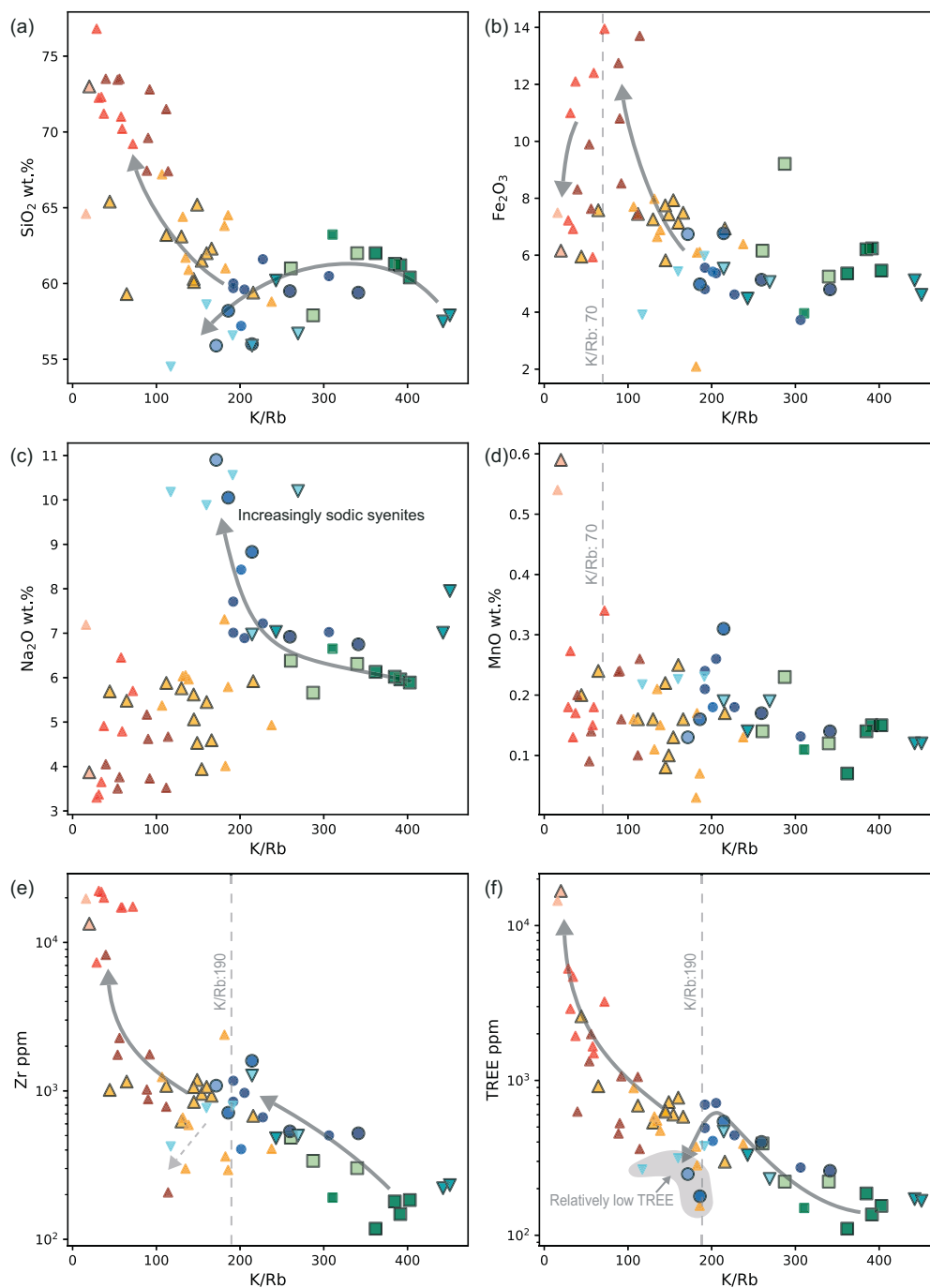


**Fig. 10.** Bivariate plots of the Ampasibitika Intrusion trends in major oxides and trace element data relative to K/Rb, which is used as an indicator of differentiation with higher values indicating less and lower values more differentiated compositions: (a)  $\text{SiO}_2$ , (b)  $\text{Fe}_2\text{O}_3$ , (c)  $\text{Na}_2\text{O}$ , (d)  $\text{MnO}$ , (e) Zr ppm, and (f) total REEs (TREE) ppm. See Fig. 9 for legend.

within the magma reservoir that are disturbed during syn-collapse processes (Kennedy & Stix, 2007). Therefore, if this is the case for the Ampasibitika Intrusion, then the ARD syenites could represent the expelled crystal mush displaced from the underlying magma reservoir into the ring dyke. Further evidence of these ARD syenites having been intruded as a crystal mush is from the petrographic textures, where interstitial assemblages have distinctly different composition to the cumulate framework. The paragenesis (Fig. 3) shows that early assemblages of alkali feldspar and calcic-clinopyroxene and

calcic-amphibole are followed by interstitial assemblages and overgrowths that are dominated by increasingly sodic phases; this is corroborated by mineral chemistry analyses (Figs 5a, 6 and 7a).

From the petrography there are at least three components of the ARD: (1) crystal mush, (2) interstitial melt associated with the crystal mush and (3) phonolitic melts that developed the phonolite dykes and trachytic-phonolite enclaves. Variable interaction of all three components has given rise to the variety of textures observed at both macro and micro scale.

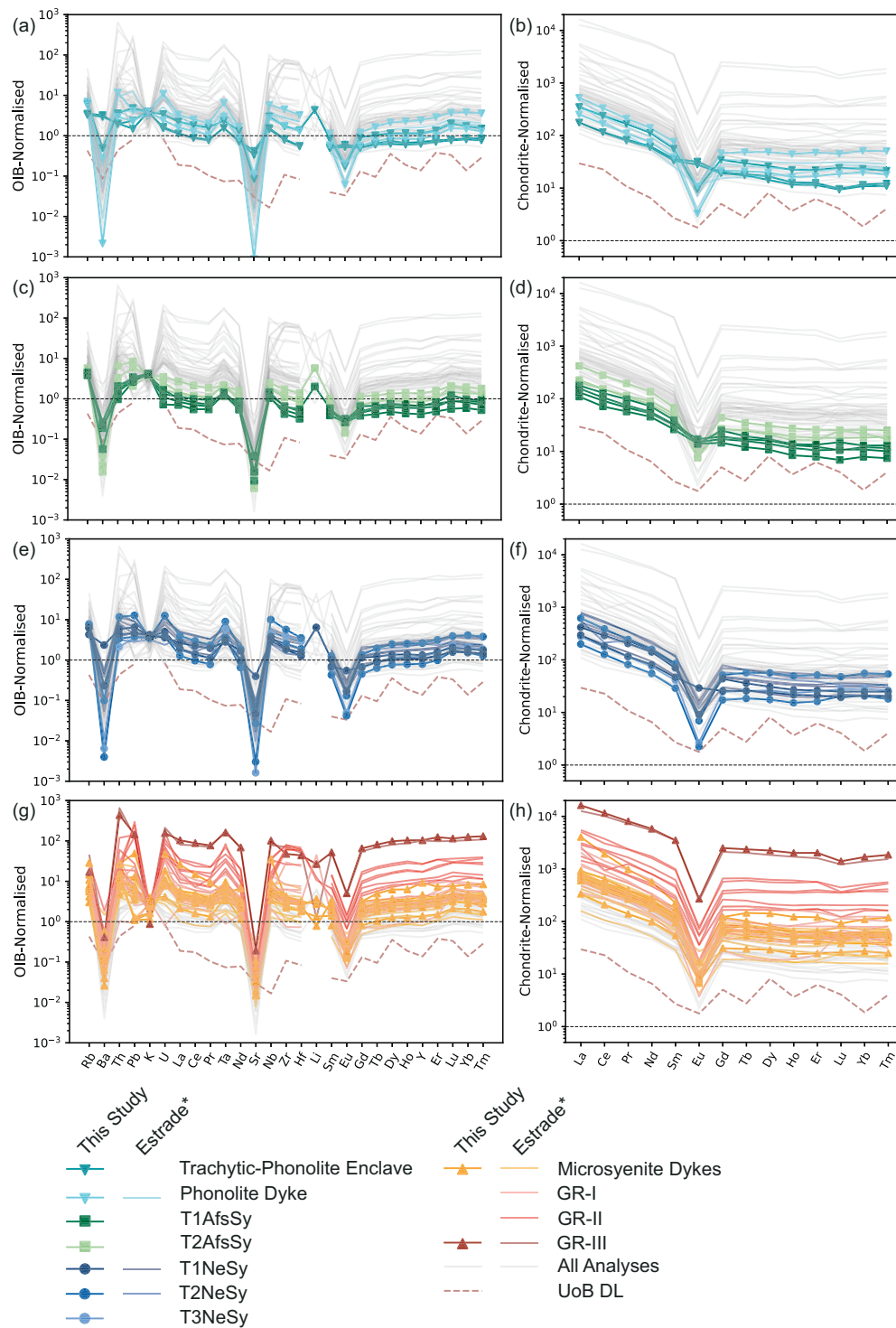


**Fig. 11.** Trace element contents normalised to OIB values of Sun & McDonough (1989) and REE contents normalised to CI Chondrite of McDonough & Sun (1995) for the Ampasibitika Intrusion (a) mafics and phonolite dykes, and trachytic-phonolite enclaves, (b) alkali feldspar syenites, (c) nepheline syenites, (d) quartz-microsyenite dykes, and (e) PGDs. Additional data from Estrade et al. (2014a, 2015). OIB normalisation was chosen for the trace element data due to the similarity in patterns of cross-cutting mafic dykes in the area, which are inferred to be the closest representative of mantle source compositions.

The dominance of cumulate alkali feldspar and calcic clinopyroxene in the T1AfsSy indicates that this represents the crystal mush with a small component of sodic interstitial melt. In contrast, the T3NeSy contains a highly sodic intracrystalline assemblage that crystallised from the interstitial melt, and also evidence of late-stage fluids carrying F, Ca and REE. The T1NeSy contains

a relatively well-developed alkali feldspar framework and Ca-amphibole, which have subsequently been resorbed and replaced by sodic and foid phases. This implies that there has been interaction of the crystal mush with a sodic interstitial melt. The implications of this interaction between the crystal mush and interstitial melt(s) are observed in the mineral chemistry, discussed below.

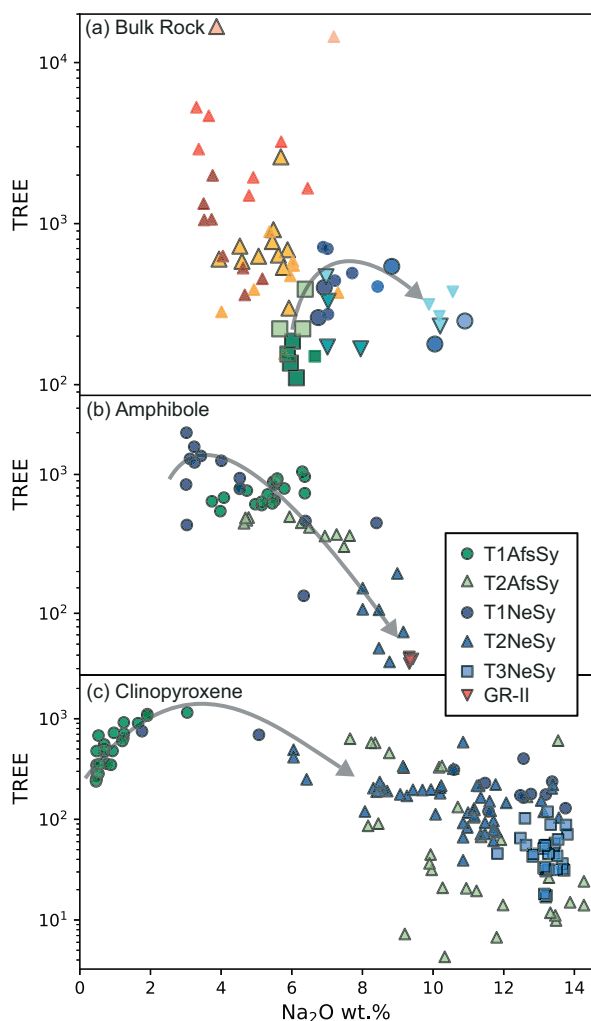


**Fig. 12.** Comparing trends in REE vs  $\text{Na}_2\text{O}$  in (a) whole rock (see Fig. 9 for legend) and ferromagnesian phases, (b) amphibole and (c) clinopyroxene. There is a general trend of initial REE enrichment with increasing Na followed by REE depletion, for syenites and their contained ferromagnesian phases, indicative of these phases exerting a strong control on REE deportment and overall REE signature of the syenites. In contrast the divergence in REE content for PGD, i.e. high REE and low  $\text{Na}_2\text{O}$  in bulk rock (a) and low REE and high  $\text{Na}_2\text{O}$  in clinopyroxene (b), indicates that ferromagnesian phases are less important contributors to REE signatures for this PGD and, by extension, the silica-oversaturated lithologies.

In the ARD, the main REE-host phases are amphiboles and pyroxenes, with early HFSE- and REE-mineral phases being accessory phases such as low REE apatite. In most cases, within the ARD syenites, the crystallisation of discrete REE and HFSE minerals, such as pyrochlore group minerals, thorite, REE-fluorocarbonates, monazite, EGM, and zircon, is associated with the development of strongly sodic assemblages and is restricted to late magmatic to hydrothermal stages of syenite evolution. This indirectly suggests that many HFSE and REE become less compatible in clinopyroxene and amphibole during progressive melt evolution. Further evidence of the shift in HFSE and REE compatibility from Ca to Na pyroxene and amphibole varieties is revealed by the trace element mineral chemistry, as sodic varieties of these phases are ubiquitously depleted in REE relative to their calcic counterparts (Fig. 12).

Investigation of trace element partitioning in clinopyroxene and amphibole in alkaline to peralkaline systems has received

increasing attention in recent years due to the apparent controls of these phases on the development and character of REE mineralisation in these systems (Marks *et al.*, 2004; Siegel *et al.*, 2017; Beard *et al.*, 2019; Vasyukova & Williams-Jones, 2019; Baudouin *et al.*, 2020; Beard *et al.*, 2020). Behaviour of REE and HFSE in both amphibole and clinopyroxene group minerals is controlled by a combination of magmatic and crystal chemical constraints. Studies of peralkaline systems have shown that Ca-rich amphibole and clinopyroxene are enriched in LREE, by up to an order of magnitude, relative to their sodic counterparts, whereas sodic variants exhibit stronger relative enrichment in HREE (Marks *et al.*, 2004; Siegel *et al.*, 2017). In general, the results presented here for amphiboles and clinopyroxenes are consistent with previous studies. As such, with the crystallisation of increasingly sodic amphibole and clinopyroxene, there is the potential to enrich residual melts and fluids in LREE.

Hedenbergite and hastingsite are early magmatic phases in the T1AfsSy and T1NeSy, respectively. These phases would have formed and sequestered REE from an early-stage melt. Negative Ba, Sr and Eu anomalies indicate that these minerals crystallised from a melt that was already relatively evolved having crystallised plagioclase and alkali feldspar. However, the crystallisation of these early magmatic REE-enriched calcic phases did not sequester all REE and HFSE and prevented subsequent enrichment of REE in later-stage melts. Crystallisation of unique REE and HFSE minerals, such as britholite, pyrochlore group minerals, REE apatite, EGM and Ca-Na-zirconosilicates (Fig. 4a–d), as late interstitial phases suggests that late-stage melts were REE and HFSE enriched. The development of REE-enriched late-stage melts could result from multiple mechanisms including the following: (1) partition coefficients between early crystallising mineral phases and the parental melt were not sufficient to deplete the melt with respect to REE and HFSE; (2) incongruent replacement of calcic phases by sodic counterparts (hedenbergite >> aegirine, hastingsite >> katophorite) released previously sequestered REE into the melt phase; and/or (3) stabilisation and crystallisation of increasingly sodic phases during the latter stages of crystallisation or in presence of a new (sodic) interstitial melt resulted in a switch from relative REE compatibility (enrichment in rock forming minerals) to REE incompatibility (enrichment in residual melt).

A peculiarity of the T3NeSy is that it is relatively depleted in REE despite a relatively evolved K/Rb signature (Figs 3e, 4c and 10f), in contrast to other peralkaline complexes where agpaite nepheline syenites are typically strongly REE enriched. This trend in decreasing REE, and to a lesser extent Zr, with decreasing K/Rb is developed in nepheline syenites and phonolites with K/Rb <190 (Fig. 10e, f). Potential explanations for this trend include the following: (a) REE previously fractionated by phases with a high affinity for REE (Kogarko *et al.*, 2002; Pfaff *et al.*, 2008; Honour *et al.*, 2018); (b) partitioning of REE into a volatile-rich residual melt/fluid after crystallisation of REE incompatible assemblages (i.e. fractional crystallisation) or (c) segregation of an immiscible melt/fluid that sequestered REE from the silicate melt (Vasyukova & Williams-Jones, 2016; Kynicky *et al.*, 2019). Within the samples assessed in this study, there is no apparent HFSE-mineral phase in the less evolved nepheline syenite samples that would actively sequester REE from the melt to account for the observed REE depletion. In addition, the presence of EGM, and fluorite-Y, within the relatively REE-depleted T3NeSy indicates that the parental melt of this evolved syenite was enriched in HFSE, and likely REE, as it is unlikely these HFSE phases would have crystallised in the absence of their major constituents. Thus, the development

of a segregated or residual volatile/ligand-rich ( $F^-$ ,  $Cl^-$ ,  $CO_3^{2-}$ ,  $OH^-$ , etc.) melt/fluid phase is the preferred explanation for the decrease in REE in the Ankobabe Hybrid nepheline syenites crystallised from evolved melts.

Experimental studies of fluorine in nepheline syenite melts show that it acts as a depolymerisation agent and enhances solubility of Zr and REE. However, unlike the REE, Zr does not form melt complexes with fluorine (Ponader & Brown, 1989a; Ponader & Brown, 1989b; Farges, 1996). Thus, development of a residual or immiscible volatile and ligand-rich phase ( $F^-$ ,  $Cl^-$ ,  $CO_3^{2-}$ ,  $OH^-$ , etc.) is a plausible explanation for the REE and Zr behaviour, with, for example, the compatibility decreases of these elements in clinopyroxene as melt  $F^-$  content increases (Beard *et al.*, 2020). Migration of a residual/segregated volatile, alkali and REE-rich phase and its subsequent accumulation may provide a mechanism for the development of the extreme REE enrichment observed in the MDS. The exact nature of this phase, immiscible melt vs exsolved fluid, remains uncertain. Tangential evidence for an immiscible melt lies within the Ankobabe Hybrid trachytic-phonolite enclaves, in which ocelli and blebs containing disseminated fluorite indicate the potential for multiple melt phases. Such immiscible melts have been proposed as a mechanism of REE enrichment in peralkaline systems (Vasyukova & Williams-Jones, 2020). However, it is beyond the scope of this study to define further if it was a melt or fluid (or both) that had the greatest influence on REE mobilisation.

### Marginal Dyke Swarm development

A key question becomes the timing of the MDS emplacement in relation to the caldera collapse event. Previous studies have interpreted the PGDs as the youngest intrusive phase of the Ampasibitika Intrusion on the basis of sparse cross-cutting relationships (Donnot, 1963; Ganzeev *et al.*, 1989; Estrade *et al.*, 2014a). However, our observations have shown that, although cross-cutting relationships can be discerned within the MDS, it is challenging to define any relationship between the MDS and ARD in field outcrops and available core. Trachytic, pegmatitic and aplitic textures of the MDS dykes are consistent with relatively rapid emplacement and crystallisation of the MDS. As such, the formation processes operating cannot be considered as equivalent, as the ARD and MDS represent different portions of the magmatic system. Focussing in on the petrography and mineral chemistry enables a refined understanding of these parts of the magmatic system.

As highlighted by Estrade *et al.* (2014a), the Ampasibitika Intrusion exhibits a de-coupled evolution between alkalinity and silica saturation (Fig. 9b). Estrade *et al.* (2014a) proposed that 'crustal contamination of the mantle-derived undersaturated magma undergoing fractional crystallisation of plagioclase and alkali feldspar is a plausible mechanism to explain the formation of the silica-oversaturated rocks'; following this assertion, the development of the GR-I, GR-II and GR-III granites were suggested to result from differing degrees of fractionation of a common basaltic parent melt (Estrade *et al.*, 2014b). However, modelling by Ballouard *et al.* (2020) of Nb-Ta enrichment in the silica-oversaturated series of the Ampasibitika Intrusion indicates that >90% fractional crystallisation of biotite and ilmenite or hydrothermal alteration is required to produce the compositions observed.

Enrichments in total REE and Zr are not proportional to the degree of differentiation indicated by K/Rb (Fig. 10e, f). The exponential enrichment in REE in the PGDs indicates that fractional crystallisation alone may not fully account for observed REE

behaviour. Although some of this behaviour could potentially result from post-emplacement hydrothermal alteration (Estrade *et al.*, 2014b), the exponential enrichment and the apparent inability of fractional crystallisation to produce the observed trends in HFSE enrichment (Ballouard *et al.*, 2020) indicate that an alternative model is required for the development of the silica saturation variability and associated changes in peralkalinity and REE enrichment.

Development of co-genetic silica-oversaturated to silica-undersaturated magmas is a feature common to a number of alkaline-peralkaline igneous complexes worldwide (e.g. Riishuus *et al.*, 2008; Marks & Markl, 2017). Generally, the mechanism invoked for such divergent co-genetic compositions is the assimilation of a silica-rich crustal material by undersaturated melts alongside fractional crystallisation trajectory (Brooks & Gill, 1982; Foland *et al.*, 1993; Estrade *et al.*, 2014a; Borst *et al.*, 2019). However, recently, more in-depth studies have investigated the type of silica-rich contaminant and mechanism of assimilation. Finch *et al.* (2019) and (Harris *et al.*, 2017) investigated the Motzfeldt (Greenland) and Straumsvola (Antarctica) complexes, respectively. These have further developed potential mechanisms for the development of silica saturation including (1) 'hot sheeted roof' zones where the accumulation of residual melts may enable flux-driven melting of silicic contaminants (Finch *et al.*, 2019) and (2) partial melting of metasomatized material as a source of silica (Harris *et al.*, 2017). In the latter case, variability in the magnitude of silica saturation has several explanations including differing degrees of subsequent fractional crystallisation, differing degrees of initial partial melting or the extent of mixing between granitic melt (derived from partial melting) and residual silica-undersaturated melt. Development and mixing of silicic partial melts, and subsequent mixing of such melts with mafic parent magma, have also been suggested as a mechanism for the generation of the spectrum of compositions observed at the Ditrău complex (Ódri *et al.*, 2020).

Volatile-rich caps are considered to be present in many peralkaline volcanic systems, typically at 4- to 6-km depth, with fluid/melt intrusions into these cap zones being a mechanism for caldera uplift (Macdonald & Scaillet, 2006; Neave *et al.*, 2012; Hutchison *et al.*, 2016a; Hutchison *et al.*, 2016b). Movement of REE, Cl, F and alkali-rich melts into a volatile-rich cap (or 'roof zone') juxtaposed against siliceous and/or metasomatized host rocks would provide an opportunity for silica saturation. Interaction of flux-rich melts with this Si contaminant could trigger Si saturation, especially if the residual melt is dominated by Na, K, REE and halogens with small amounts of 'major' elements (Al, Si). This would require a relatively small amount of Si contamination to develop silica saturation in the GR-III PGD, whilst also accounting for the strongly peralkaline and REE signature of these dykes. Variable degrees of contamination and interaction of flux-rich melts, syenitic melts in the roof zone and assimilation of silicic material could account for the range in composition of the MDS. With greater degrees of contamination and homogenisation potentially resulting in the observed decreasing silica saturation, peralkalinity and REE concentrations, as a result of dilution effects (Fig. 13).

### Implications for REE mineralisation

The mineralogy of each intrusive unit is a function of the preceding evolution of the melts and mushes within the underlying magma reservoir. As such, the final distribution of REE mineralisation is also a function of these magmatic and emplacement processes.

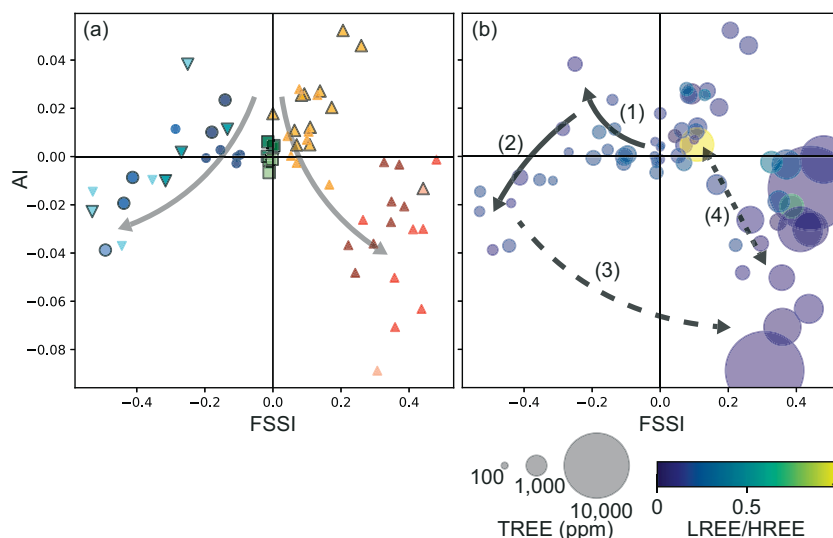


**Fig. 13.** Interpretations of alkalinity index (AI—see Fig. 9) vs feldspathoid silica saturation index (FSSI—see Fig. 9) trends for the Ampasibitika Intrusion: (a) there is a clear divergence in AI vs FSSI during differentiation of the (1) silica-undersaturated and (2) silica-oversaturated series of the Ampasibitika Intrusion (Estrade *et al.*, 2014a)—for legend see Fig. 9. (b) If an integrated view of these units is taken, then the changing REE concentrations depending on lithology and location in the magma reservoir (Fig. 14) could reflect the following: (1) initial REE accumulation in calcic ferromagnesian phases, (2) REE incompatibility and concentration in residual melts, (3) fluid/melt from magma reservoir accumulating in volatile cap and (4) variable homogenization with syenitic melts and Si contaminant in roof zone.

Development of relatively REE-poor, highly sodic, agpaitic syenites has implications for the compositions of residual melts that have the potential to accumulate in the roof zone. At extreme stages of melt evolution, there are likely switches in compatibility related to changes in mineral-melt partitioning (Möller & Williams-Jones, 2016a) and the availability of major elements. The development of increasingly sodic interstitial assemblages is noted to be at the expense of previously crystallised calcic counterparts. This indicates that at the latest stages of melt evolution, previously compatible elements, such as Ca, Mn and, to a lesser extent, REE behave in an increasingly incompatible manner. Tangential evidence for this is the presence of late veinlets in the T3NeSy comprising fluorite-Y ( $\text{CaF}_2$ ) and Mn phases (Fig. 4d). During the later stages of crystallisation, sodic phases dominate over their potassic counterparts, as observed in whole rock chemistry, as a result of nepheline and aegirine accumulation. This could indicate that either K has been effectively sequestered by earlier crystallised phases or the dominance of aegirine as the primary ferromagnesian phase during these later stages of crystallisation has resulted in K being sequestered into a melt/fluid phase. As such, it is proposed that during melt evolution there is a progression to increasingly volatile rich (F, Cl), Si and Al poor, and  $\text{K} > \text{Na}$ , and slightly Ca- and Mn-enriched residual melt/fluids that sequestered REE. If these melts remained *in situ*, the final agpaitic assemblages could have resembled those documented at Ilímaussaq (Marks & Markl, 2015) and Nechalacho Layered Suite (Möller & Williams-Jones, 2016a; Möller & Williams-Jones, 2016b). Conversely, migration of these melts into a volatile cap—as invoked to be present for the Ampasibitika Intrusion—could provide a source of REE and volatiles for PGD development.

Due to the accumulation of REE and volatiles within the roof zone, it is the MDS that contains the PGD with the highest REE concentrations. However, the MDS does not have consistently high REE concentration with a spectrum from most REE-enriched GR-III to the least REE-enriched microsyenite dykes. This transition is also accompanied by changes in mineralogy, with progressively increasing proportions of alkali feldspar and a change

from agpaitic mineral assemblages, to miaskitic mineral assemblages, with the microsyenite dykes containing a range of REE-fluorocarbonate phases. In regolith profiles associated with these lithologies it is noted that, although the highest total REE contents are associated with the PGD, the proportion of ion exchangeable REE is relatively low, reflecting the protolith mineralogy, with a significant portion of REE hosted in low solubility zirconosilicates (Estrade *et al.*, 2019).

In contrast, although the ARD syenites are generally less REE enriched than the MDS, the availability of REE for release and subsequent adsorption within regolith profiles is more favourable, as both pyroxene and amphibole are major REE-host phases within these syenites and are susceptible to breakdown and dissolution during weathering processes. That said, there is a hierarchy of availability, as syenites with less evolved compositions (i.e. T1NeSy and T1AfsSy) contain a greater proportion of REE within their calcic amphiboles and pyroxenes, relative to the more evolved T2NeSy, T3NeSy and T2AfsSy, that are dominated by more sodic assemblages and often have more specific HFSE- and REE-mineral phases.

Thus, by this argument, one of the most favourable source rocks for the development of ion adsorption ores in the Ampasibitika area is the T1AfsSy; although this syenite is not especially REE enriched, it contained a significant proportion of its REE budget in a form that was available for ion adsorption mineralisation development. Whereas in the highly evolved PGD, although having high total REE contents, the availability of REE for IADs is reduced.

In actuality, there are a number of other factors that must also be considered. From this study, and Estrade *et al.* (2019), the total REE availability is still a major control. For example, even if the GR-III releases 5% of its total REE budget to the ion adsorption ores, with a whole rock REE content of c. 16 000 ppm, the total REE released is still greater than a T1AfsSy, with a whole rock REE content of 306 ppm releasing 50% of its REE budget. In addition, controls are exerted by regolith mineralogical and physical composition, which dictates the porosity and permeability of the protolith, and topographic controls on regolith development, which

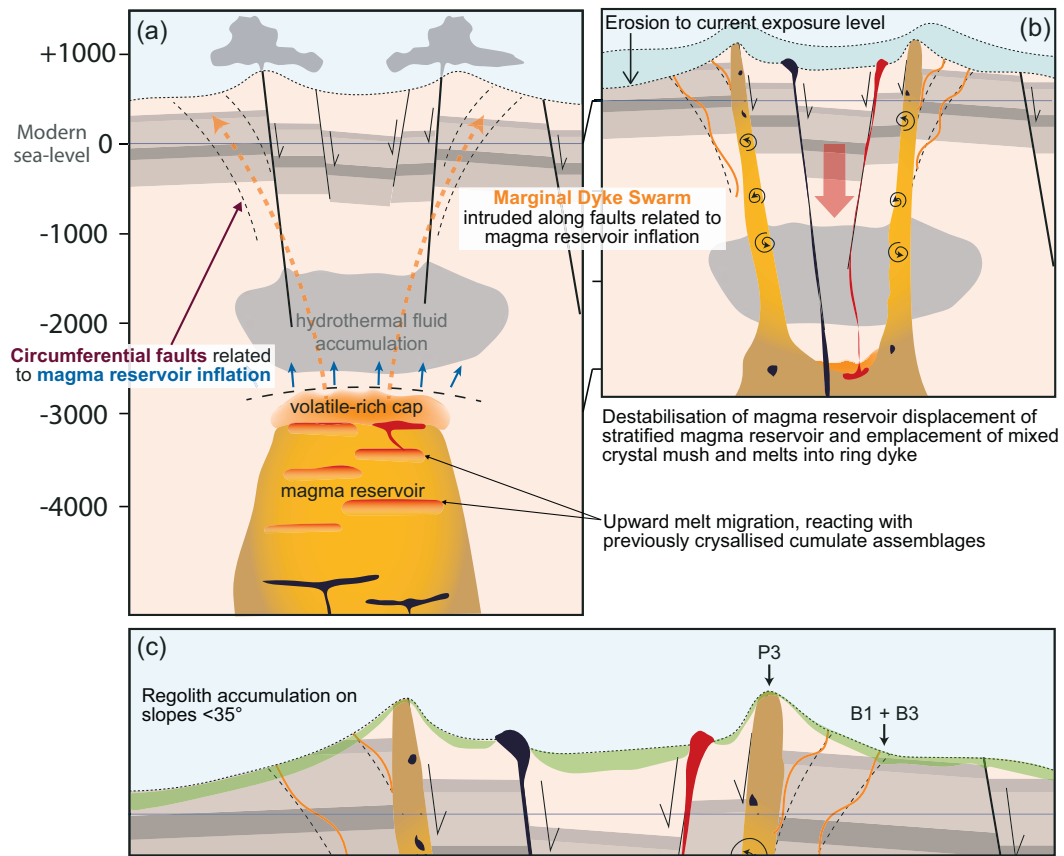


**Fig. 14.** It is envisaged that the parental magma reservoir of the Ampasibitika Annular Intrusion was stratified, similar to that hypothesised for the Aluto volcano in Ethiopia by Hutchison *et al.* (2016a). A key characteristic is the presence of a volatile-rich cap overlying the magma reservoir comprising silica-undersaturated melts. (a) The progressive development of increasingly sodic mineral assemblages, without crystallisation of significant volumes of HFSE/REE minerals, indicates residual melts/fluids were progressively enriched in REE (and volatiles). Upwards migration of volatile-rich melts and/or fluids transport HFSE and REE upwards into the volatile cap zone—this zone of volatile, REE-rich melts are the precursors for the MDS peralkaline granite and microsyenite dykes, with variable degrees of interaction of these with silicic and feldspathic contaminants resulting in the range in compositions observed (Fig. 13b). (b) Destabilisation and overturning of the underlying magma reservoir triggered caldera collapse and the emplacement of the heterogeneous silica-neutral to silica-undersaturated ARD. Vortices developed during emplacement, and differing degrees of crystal-network development within crystal mushes, led to the range of magma mingling textures observed (Fig. 2a–c). (c) The magmatic and emplacement history of the Ampasibitika Intrusion resulted in the stark divisions between the silica-oversaturated, highly REE-enriched MDS and the less REE-enriched silica-neutral to silica-undersaturated syenites of the ARD. Differences in the REE department within different mineral assemblages and total REE contents lead to the variable development of ion adsorption mineralisation, as described by Estrade *et al.* (2019) (P1, B1 + B3, relate to regolith profiles assessed by Estrade *et al.*, 2019).

control the thickness of weathering profiles and the hydrogeology (Estrade *et al.*, 2019).

## CONCLUSIONS—OVERALL EMPLACEMENT MODEL AND IMPACT ON MINERALISATION

On the basis of field relations, bulk rock and microscale geochemistry, we propose an expansion of the current model for development of the silica-undersaturated to silica-oversaturated, variably REE-enriched, and peralkaline Ampasibitika Intrusion. We demonstrate the importance of magma mixing and mingling at the hypabyssal level during peralkaline caldera collapse. We also infer that models of REE enrichment at late stages of magma crystallisation by separation of a volatile-enriched residual melt or fluid phase developed for plutonic alkaline complexes are also applicable, and may be particularly important, at hypabyssal levels.

Parental magmas of the Ampasibitika Intrusion are considered to have been of alkali basalt or basanitic composition (Estrade *et al.*, 2014a; Cucciniello *et al.*, 2016). Fractionation of plagioclase, alkali feldspar, Fe–Ti-oxides or rutile, and apatite led to the devel-

opment of more evolved alkaline magmas such as trachytes and phonolites (Estrade *et al.*, 2014a; Cucciniello *et al.*, 2016). These evolved melts were emplaced at shallower crustal levels (Beard *et al.*, 2022) leading to the formation of the magma reservoir for the Ampasibitika Intrusion (Fig. 14).

Based on the field relationships and petrographic relationships observed, we propose that the magma reservoir that underlay the Ampasibitika Intrusion comprised a crystal mush capped by a melt-dominated roof zone (Fig. 14). Upwards migration of melt lenses within the underlying crystal mushes resulted in the development of alkali-bearing, increasingly REE and volatile-rich residual melts, which segregated, leaving behind REE-poor, apatitic syenites. Accumulation of the segregated REE, alkali and volatile-rich residual melts within a volatile-rich cap/roof zone, juxtaposed against silicic-host rock resulted in silica saturation. Variable degrees of partial melting, mixing and homogenisation resulted in the variable compositions of the MDS. This activity in the roof zone may have also been responsible for caldera inflation and development of circumferential faults, which the MDS melts exploited. Following planes of structural weakness, these melts transferred from the roof zone of the magma reservoir

to sub-volcanic levels where they rapidly crystallised to preserve the heterogeneous and variably REE-enriched microsyenites and peralkaline granites.

Destabilisation of the crystal mush-rich magma reservoir and caldera collapse led to the emplacement of the ARD within the main ring dyke. Rapid emplacement of a range of melts and mushes led to the magma mingling textures observed in the Ankobabe Hybrids. Dominated by alkali feldspar networks, the interstitial assemblage of these syenites varies considerably, indicating the presence of a highly heterogeneous magma reservoir with lenses of relatively calcic to sodic fractions. Transitory melt lenses are thought to account for the differing compositions between the early crystallised mineral framework and interstitial assemblages observed in some syenites. The development of highly sodic, apatitic assemblages is suggested to have been accompanied by segregation of REE-rich melts/fluids resulting in relatively low whole rock REE concentrations in the T3NeSy. Contribution of such fluids to the volatile cap could potentially provide a REE-rich, relatively Al- and Si-poor, and  $K > Na$  source for development of the GR-III PGDs.

The distribution of these magma reservoir components on emplacement was controlled by caldera collapse processes. Initial emplacement of the low-viscosity MDS is inferred to have occurred during magma reservoir inflation and emplacement into marginal, concentric fractures surrounding a dome; subsequent caldera collapse would enable displacement and transport of crystal mushes from the magma reservoir into the ring dyke structure.

Syenites of the ARD host REE predominantly within major rock forming minerals, such as amphibole and clinopyroxene, whereas within the marginal dykes, REEs are typically hosted in HFSE/REE-mineral phases (e.g. EGM, pyrochlore group minerals, zircon). The main mineral phases within the latter are less susceptible to breakdown and dissolution during weathering. As such, although more REE enriched, the proportion of easily exchangeable REE within the resultant weathered profiles is less for those developed from PGD relative to ARD syenites (Estrade *et al.*, 2019). Therefore, the distribution of REE within the regolith and development of ion adsorption-style mineralisation is controlled in part by the magmatic, hydrothermal and emplacement evolution of the protoliths.

## DATA AVAILABILITY

The data underlying this article are available in the article and in its online supplementary material.

## SUPPLEMENTARY DATA

Supplementary data are available at *Journal of Petrology* online.

## ACKNOWLEDGEMENTS

Rocky Lowell Rakotoson and Fetra Rasolonirina are thanked for their invaluable assistance in organising fieldwork and field expertise in Madagascar. Tantalus Rare Earths AG provided assistance with field logistics and access to the drill core. Pete Lyons and Dr Magda Grove provided assistance and support in the development of ICP-MS procedures at the University of Brighton. Joe Pickles and Gavyn Rollinson enabled access and provided assistance in the collection of EMP dataset at the Chemical, Imaging and Mineralogical Facility (CIMF), Camborne School of Mines, University of Exeter. The British Geological

Survey's Charles Gowning and John Wheeler provided access and assistance to the BGS rock crushing facilities; Gren Turner, Alicja Lacinska and Jeremy Rushton provided assistance and expertise for SEM imagery collection; and Simon Chenery provided assistance and expertise during the collection of LA-ICP-MS datasets. This paper is a product of the SoS RARE project, which is funded by the UK's Natural Environment Research Council under grant agreement no. NE/M011429/1.

## References

- Andersen, T., Elburg, M. & Erambert, M. (2017). The miaskitic-to-agpaitic transition in peralkaline nepheline syenite (white foyaitite) from the Pilanesberg complex, South Africa. *Chemical Geology* **455**, 166–181. <https://doi.org/10.1016/j.chemgeo.2016.08.020>.
- Armistead, S. E., Collins, A. S., Merdith, A. S., Payne, J. L., Cox, G. M., Foden, J. D., Razakamanana, T. & De Waele, B. (2019). Evolving marginal terranes during Neoproterozoic supercontinent reorganization: constraints from the Bemarivo Domain in northern Madagascar. *Tectonics* **38**, 2019–2035. <https://doi.org/10.1029/2018TC005384>.
- Armistead, S. E., Collins, A. S., Redaa, A., Jepson, G., Gillespie, J., Gilbert, S., Blades, M. L., Foden, J. D. & Razakamanana, T. (2020). Structural evolution and medium-temperature thermochronology of central Madagascar: implications for Gondwana amalgamation. *Journal of the Geological Society* **177**, 784–798. <https://doi.org/10.1144/jgs2019-132>.
- ASTER GDEM (2011) Advanced spaceborne thermal emission and reflection radiometer (Aster) global digital elevation model (GDEM). Version 2 [dataset: ASTGTM2\_S14E047, ASTGTM2\_S14E048, ASTGTM2\_S15E047, ASTGTM2\_S15E048]. NASA/METI/AIST/Japan Spacesystems & US/Japan ASTER Science Team. <https://lpdaac.usgs.gov/products/astgtmv002/> (accessed on 4 June 2019).
- Ballouard, C., Massuyeau, M., Elburg, M. A., Tappe, S., Viljoen, F. & Brandenburg, J.-T. (2020). The magmatic and magmatic-hydrothermal evolution of felsic igneous rocks as seen through Nb-Ta geochemical fractionation, with implications for the origins of rare-metal mineralizations. *Earth-Science Reviews* **203**, 103115. <https://doi.org/10.1016/j.earscirev.2020.103115>.
- Bao, Z. & Zhao, Z. (2008). Geochemistry of mineralization with exchangeable REY in the weathering crusts of granitic rocks in South China. *Ore Geology Reviews* **33**, 519–535. <https://doi.org/10.1016/j.oregeorev.2007.03.005>.
- Barbarin, B. (2005). Mafic magmatic enclaves and mafic rocks associated with some granitoids of the central Sierra Nevada batholith, California: nature, origin, and relations with the hosts. *Lithos* **80**, 155–177. <https://doi.org/10.1016/j.lithos.2004.05.010>.
- Barbarin, B. & Didier, J. (1992). Genesis and evolution of mafic microgranular enclaves through various types of interaction between coexisting felsic and mafic magmas. *Earth and Environmental Science Transactions of the Royal Society of Edinburgh* **83**, 145–153. <https://doi.org/10.1017/S0263593300007835>.
- Baudouin, C., France, L., Boulanger, M., Dalou, C. & Devidal, J.-L. (2020). Trace element partitioning between clinopyroxene and alkaline magmas: parametrization and role of M1 site on HREE enrichment in clinopyroxenes. *Contributions to Mineralogy and Petrology* **175**, 42. <https://doi.org/10.1007/s00410-020-01680-6>.
- Beard, C. D., van Hinsberg, V. J., Stix, J. & Wilke, M. (2019). Clinopyroxene/melt trace element partitioning in sodic alkaline magmas. *Journal of Petrology* **60**, 1797–1823. <https://doi.org/10.1093/petrology/egz052>.
- Beard, C. D., van Hinsberg, V. J., Stix, J. & Wilke, M. (2020). The effect of fluorine on clinopyroxene/melt trace-element

- partitioning. *Contributions to Mineralogy and Petrology* **175**, 44. <https://doi.org/10.1007/s00410-020-1672-5>.
- Beard, C. D., Goodenough, K. M., Borst, A. M., Wall, F., Siegfried, P. R., Deady, E. A., Pohl, C., Hutchison, W., Finch, A. A., Walter, B. F., Elliott, H. A. L. & Brauch, K. (2023). Alkaline-silicate REE-HFSE systems. *Economic Geology* **118**, 177–208. <https://doi.org/10.5382/econgeo.4956>.
- BGS-USGS-GLW (2008). République de Madagascar ministère de l'énergie et des mines (MEM/SG/DG/UCP/PGRM). *British Geological Survey Research Report*, 1049.
- Borst, A. M., Friis, H., Andersen, T., Nielsen, T. F. D., Waight, T. E. & Smit, M. A. (2016). Zirconosilicates in the kakortokites of the Ilímaussaq complex, South Greenland: implications for fluid evolution and high-field-strength and rare-earth element mineralization in agpaite systems. *Mineralogical Magazine* **80**, 5–30. <https://doi.org/10.1180/minmag.2016.080.046>.
- Borst, A. M., Waight, T. E., Finch, A. A., Storey, M. & Roux, P. L. (2019). Dating agpaite rocks: a multi-system (U/Pb, Sm/Nd, Rb/Sr and  $^{40}\text{Ar}/^{39}\text{Ar}$ ) isotopic study of layered nepheline syenites from the Ilímaussaq complex, Greenland. *Lithos* **324–325**, 74–88. <https://doi.org/10.1016/j.lithos.2018.10.037>.
- Borst, A. M., Smith, M. P., Finch, A. A., Estrade, G. E., Villanova-de-Benevent, C., Nason, P., Marquis, E., Horsburgh, N. J., Goodenough, K. M., Xu, C., Kynický, J. & Geraki, K. (2020). Adsorption of rare earth elements in regolith-hosted clay deposits. *Nature Communications* **11**, 4386. <https://doi.org/10.1038/s41467-020-17801-5>.
- Brooks, C. & Gill, R. (1982). Compositional variation in the pyroxenes and amphiboles of the Kangerdlugssuaq intrusion, East Greenland: further evidence for the crustal contamination of syenite magma. *Mineralogical Magazine* **45**, 1–9. <https://doi.org/10.1180/minmag.1982.045.337.01>.
- Cawthorn, R. G. (2015). The geometry and emplacement of the Pilanesberg Complex, South Africa. *Geological Magazine* **152**, 802–812. <https://doi.org/10.1017/S0016756814000764>.
- Collins, A. S. (2006). Madagascar and the amalgamation of Central Gondwana. *Gondwana Research* **9**, 3–16. <https://doi.org/10.1016/j.gr.2005.10.001>.
- Collins, A. S. & Pisarevsky, S. A. (2005). Amalgamating eastern Gondwana: the evolution of the Circum-Indian Orogens. *Earth-Science Reviews* **71**, 229–270. <https://doi.org/10.1016/j.earscirev.2005.02.004>.
- Cucciniello, C., Melluso, L., Morra, V., Storey, M., Rocco, I., Franciosi, L., Grifa, C., Petrone, C. & Vincent, M. (2011). New  $^{40}\text{Ar}/^{39}\text{Ar}$  ages and petrogenesis of the Massif d'Ambre volcano, northern Madagascar. *Geological Society of America Special Papers* **478**, 257–281.
- Cucciniello, C., Tucker, R. D., Jourdan, F., Melluso, L. & Morra, V. (2016). The age and petrogenesis of alkaline magmatism in the Ampasindava Peninsula and Nosy Be archipelago, northern Madagascar. *Mineralogy and Petrology* **110**, 309–331. <https://doi.org/10.1007/s00710-015-0387-1>.
- Desharnais, G., Camus, Y. & Bisailon, C. (2014) NI 43–101 Technical Report on Resources for the Tantalus Rare Earth Ionic Clay Project, Northern Madagascar, Prepared for Tantalus Rare Earths AG. SGS.
- Ding, J.-Y. & Deng, G.-Q. (2013). Main problems in the current ionic adsorption rare earth exploration specifications and their amendment proposals. *Nonferrous Metals Science and Engineering* **4**, 96–102.
- Donnot, M. (1963) *Les complexes intrusifs alcalins de la province pétrographique d'Ampasindava et leurs minéralisations*. BRGM, Madagascar.
- Elburg, M. A. & Cawthorn, R. G. (2017). Source and evolution of the alkaline Pilanesberg Complex, South Africa. *Chemical Geology* **455**, 148–165. <https://doi.org/10.1016/j.chemgeo.2016.10.007>.
- Emerick, C. M. & Duncan, R. A. (1982). Age progressive volcanism in the Comores Archipelago, western Indian Ocean and implications for Somali plate tectonics. *Earth and Planetary Science Letters* **60**, 415–428. [https://doi.org/10.1016/0012-821X\(82\)90077-2](https://doi.org/10.1016/0012-821X(82)90077-2).
- Estrade, G., Béziat, D., Salvi, S., Tiepolo, M., Paquette, J.-L. & Rakotovo, S. (2014a). Unusual evolution of silica-under- and -oversaturated alkaline rocks in the Cenozoic Ambohimirahavavy Complex (Madagascar): mineralogical and geochemical evidence. *Lithos* **206–207**, 361–383. <https://doi.org/10.1016/j.lithos.2014.08.008>.
- Estrade, G., Salvi, S., Béziat, D., Rakotovo, S. & Rakotondrazafy, R. (2014b). REE and HFSE mineralization in peralkaline granites of the Ambohimirahavavy alkaline complex, Ampasindava peninsula, Madagascar. *Journal of African Earth Sciences* **94**, 141–155. <https://doi.org/10.1016/j.jafrearsci.2013.06.008>.
- Estrade, G., Salvi, S., Béziat, D. & Williams-Jones, A. E. (2015). The origin of Skarn-hosted rare-metal mineralization in the Ambohimirahavavy alkaline complex, Madagascar. *Economic Geology* **110**, 1485–1513. <https://doi.org/10.2113/econgeo.110.6.1485>.
- Estrade, G., Salvi, S. & Béziat, D. (2018). Crystallization and destabilization of eudialyte-group minerals in peralkaline granite and pegmatite: a case study from the Ambohimirahavavy complex, Madagascar. *Mineralogical Magazine* **82**, 375–399. <https://doi.org/10.1180/minmag.2017.081.053>.
- Estrade, G., Marquis, E., Smith, M. P., Nason, P. & Goodenough, K. M. (2019). REE concentration processes in ion adsorption deposits: evidence from the Ambohimirahavavy alkaline complex in Madagascar. *Ore Geology Reviews* **112**, 103027. <https://doi.org/10.1016/j.oregeorev.2019.103027>.
- European Commission (2020) *Study on the EU's list of Critical Raw Materials (2020)*. European Commission, Brussels.
- Farges, F. (1996). Does Zr-F “complexation” occur in magmas? *Chemical Geology* **127**, 253–268. [https://doi.org/10.1016/0009-2541\(95\)00132-8](https://doi.org/10.1016/0009-2541(95)00132-8).
- Finch, A. A., McCreath, J. A., Reekie, C. D. J., Hutchison, W., Ismaila, A., Armour-Brown, A., Andersen, T. & Simonsen, S. L. (2019). From mantle to Motzfeldt: a genetic model for syenite-hosted Ta,Nb-mineralisation. *Ore Geology Reviews* **107**, 402–416. <https://doi.org/10.1016/j.oregeorev.2019.02.032>.
- Foland, K., Landoll, J., Henderson, C. & Chen, J. (1993). Formation of cogenetic quartz and nepheline syenites. *Geochimica et Cosmochimica Acta* **57**, 697–704. [https://doi.org/10.1016/0016-7037\(93\)90380-F](https://doi.org/10.1016/0016-7037(93)90380-F).
- Frost, B. R. & Frost, C. D. (2008). A geochemical classification for Feldspathic igneous rocks. *Journal of Petrology* **49**, 1955–1969. <https://doi.org/10.1093/petrology/egn054>.
- Ganzev, A. A. & Grechishchev, O. K. (2003). A new genetic type of rare-metal alkali granites of Madagascar. *Russian Geology and Geophysics* **44**, 539–553.
- Ganzev, A., Raobadia, J. & Panfilov, R. (1989) *Résultats des travaux de recherches réalisés en 1989 dans la province d'Ampasindava*. Antananarivo: OMNIS.
- Goodenough, K. M., Upton, B. G. J. & Ellam, R. M. (2000). Geochemical evolution of the Ivigtut granite, South Greenland: a fluorine-rich “A-type” intrusion. *Lithos* **51**, 205–221. [https://doi.org/10.1016/S0024-4937\(99\)00064-X](https://doi.org/10.1016/S0024-4937(99)00064-X).
- Goodenough, K. M., Thomas, R. J., De Waele, B., Key, R. M., Schofield, D. I., Bauer, W., Tucker, R. D., Rafahatelo, J. M., Rabarimanana, M., Ralison, A. V. & Randriamananjara, T. (2010). Post-collisional magmatism in the central East African Orogen: the Maevarano Suite of North Madagascar. *Lithos* **116**, 18–34. <https://doi.org/10.1016/j.lithos.2009.12.005>.

- Goodenough, K. M., Wall, F. & Merriman, D. (2018). The rare earth elements: demand, global resources, and challenges for resourcing future generations. *Natural Resources Research* **27**, 201–216. <https://doi.org/10.1007/s11053-017-9336-5>.
- Harris, C., Dreyer, T. & le Roux, P. (2017). Petrogenesis of peralkaline granite dykes of the Straumsvola complex, western Dronning Maud Land, Antarctica. *Contributions to Mineralogy and Petrology* **173**, 1–24. <https://doi.org/10.1007/s00410-017-1433-2>.
- Hawthorne, F. C., Oberti, R., Harlow, G. E., Maresch, W. V., Martin, R. F., Schumacher, J. C. & Welch, M. D. (2012). Nomenclature of the amphibole supergroup. *American Mineralogist* **97**, 2031–2048. <https://doi.org/10.2138/am.2012.4276>.
- Honour, V. C., Goodenough, K. M., Shaw, R. A., Gabudianu, I. & Hirtopan, P. (2018). REE mineralisation within the Ditrău Alkaline Complex, Romania: interplay of magmatic and hydrothermal processes. *Lithos* **314–315**, 360–381. <https://doi.org/10.1016/j.lithos.2018.05.029>.
- Hutchison, W., Biggs, J., Mather, T. A., Pyle, D. M., Lewi, E., Yirgu, G., Caliro, S., Chiodini, G., Clor, L. E. & Fischer, T. P. (2016a). Causes of unrest at silicic calderas in the East African Rift: new constraints from InSAR and soil-gas chemistry at Aluto volcano, Ethiopia. *Geochemistry, Geophysics, Geosystems* **17**, 3008–3030. <https://doi.org/10.1002/2016GC006395>.
- Hutchison, W., Pyle, D. M., Mather, T. A., Yirgu, G., Biggs, J., Cohen, B. E., Barfod, D. N. & Lewi, E. (2016b). The eruptive history and magmatic evolution of Aluto volcano: new insights into silicic peralkaline volcanism in the Ethiopian rift. *Journal of Volcanology and Geothermal Research* **328**, 9–33. <https://doi.org/10.1016/j.jvolgeores.2016.09.010>.
- Jowitt, S. (2018). Introduction to a resources special issue on criticality of the rare earth elements: current and future sources and recycling. **7**, 35. <https://doi.org/10.3390/resources7020035>.
- Jowitt, S. M., Medlin, C. C. & Cas, R. A. F. (2017). The rare earth element (REE) mineralisation potential of highly fractionated rhyolites: a potential low-grade, bulk tonnage source of critical metals. *Ore Geology Reviews* **86**, 548–562. <https://doi.org/10.1016/j.oregeorev.2017.02.027>.
- Kennedy, B. & Stix, J. (2007). Magmatic processes associated with caldera collapse at Ossipee ring dyke, New Hampshire. *GSA Bulletin* **119**, 3–17. <https://doi.org/10.1130/B25980.1>.
- Kennedy, B. M., Holohan, E. P., Stix, J., Gravelly, D. M., Davidson, J. R. J. & Cole, J. W. (2018). Magma plumbing beneath collapse caldera volcanic systems. *Earth-Science Reviews* **177**, 404–424. <https://doi.org/10.1016/j.earscirev.2017.12.002>.
- Key, R. M., Pitfield, P. E. J., Thomas, R. J., Goodenough, K. M., De Waele, B., Schofield, D. I., Bauer, W., Horstwood, M. S. A., Styles, M. T., Conrad, J., Encarnacion, J., Lidke, D. J., O'Connor, E. A., Potter, C., Smith, R. A., Walsh, G. J., Ralison, A. V., Randriamananjara, T., Rafahatelo, J. M. & Rabarimanana, M. (2011). Polyphase Neoproterozoic orogenesis within the East Africa–Antarctica Orogenic Belt in central and northern Madagascar. In: van Hinsbergen D. J. J., Buiter S. J. H., Torsvik T. H., Gaina C. & Webb S. J. (eds) *The formation and evolution of Africa: A synopsis of 3.8 Ga of Earth history*. Geological Society of London, 49–68.
- Kogarko, L., Williams, C. & Woolley, A. (2002). Chemical evolution and petrogenetic implications of loparite in the layered, agpaitic Lovozero complex, Kola Peninsula, Russia. *Mineralogy and Petrology* **74**, 1–24. <https://doi.org/10.1007/s710-002-8213-2>.
- Kynicky, J., Smith, M. P., Song, W., Chakhmouradian, A. R., Xu, C., Kopriva, A., Galiova, M. V. & Brtnicky, M. (2019). The role of carbonate-fluoride melt immiscibility in shallow REE deposit evolution. *Geoscience Frontiers* **10**, 527–537. <https://doi.org/10.1016/j.gsf.2018.02.005>.
- Lacroix, A. (1902) *Matériaux pour la minéralogie de Madagascar: Les roches alcalines caractérisant la province pétrographique d'Ampasindava*, Masson et Cie ed. Paris, France.
- Lacroix, A. (1915) Sur un type nouveau de roche granitique alcaline, renfermant une eucolite. *Comptes Rendus Hebdomadaires des Seances de l'Academie des Sciences*, 253–258.
- Le Maitre, R. W., Streckeisen, A., Zanettin, B., Le Bas, M., Bonin, B., Bateman, P., Bellieni, G., Dudek, A., Efremova, A. & Keller, J. (2002) *Igneous rocks. A classification and glossary of terms*. In: Le Maitre, R.W. (Ed.), *Recommendations of the IUGS Subcommission on the Systematics of Igneous Rocks*. Cambridge: Cambridge University Press.
- Li, Y. H. M., Zhao, W. W. & Zhou, M.-F. (2017). Nature of parent rocks, mineralization styles and ore genesis of regolith-hosted REE deposits in South China: an integrated genetic model. *Journal of Asian Earth Sciences* **148**, 65–95. <https://doi.org/10.1016/j.jseaes.2017.08.004>.
- Li, M. Y. H., Zhou, M.-F. & Williams-Jones, A. E. (2019). The genesis of regolith-hosted heavy rare earth element deposits: insights from the world-class Zudong deposit in Jiangxi Province, South China. *Economic Geology* **114**, 541–568. <https://doi.org/10.5382/econgeo.4642>.
- Locock, A. J. (2014). An excel spreadsheet to classify chemical analyses of amphiboles following the IMA 2012 recommendations. *Computers & Geosciences* **62**, 1–11. <https://doi.org/10.1016/j.cageo.2013.09.011>.
- Lottermoser, B. G. (1990). Rare-earth element mineralisation within the Mt. Weld carbonatite laterite, Western Australia. *Lithos* **24**, 151–167. [https://doi.org/10.1016/0024-4937\(90\)90022-S](https://doi.org/10.1016/0024-4937(90)90022-S).
- Lusty, P. J. A., Shaw, R. A., Gunn, A. G. & Idoine, N. E. (2021) UK criticality assessment of technology critical minerals and metals. In: Bloodworth, A. J., (Ed.), *British Geological Survey Commissioned Report CR/21/120*. Keyworth, Nottingham: British Geological Survey, p.76.
- Macdonald, R. & Scaillet, B. (2006). The central Kenya peralkaline province: insights into the evolution of peralkaline salic magmas. *Lithos* **91**, 59–73. <https://doi.org/10.1016/j.lithos.2006.03.009>.
- Marks, M. & Markl, G. (2003). Ilimaussaq 'en miniature': closed-system fractionation in an agpaitic dyke rock from the Gardar Province, South Greenland (contribution to the mineralogy of Ilimaussaq no.117). *Mineralogical Magazine* **67**, 893–919. <https://doi.org/10.1180/0026461036750150>.
- Marks, M. & Markl, G. (2015) The Ilimaussaq Alkaline Complex, South Greenland. In: Charlier B., Namur O., Latypov R. & Tegner C. (eds) *Layered Intrusions*. Dordrecht: Springer, pp.649–691.
- Marks, M. & Markl, G. (2017). A global review on agpaitic rocks. *Earth-Science Reviews* **173**, 229–258. <https://doi.org/10.1016/j.earscirev.2017.06.002>.
- Marks, M., Halama, R., Wenzel, T. & Markl, G. (2004). Trace element variations in clinopyroxene and amphibole from alkaline to peralkaline syenites and granites: implications for mineral-melt trace-element partitioning. *Chemical Geology* **211**, 185–215. <https://doi.org/10.1016/j.chemgeo.2004.06.032>.
- McDonough, W. F. & Sun, S.-S. (1995). The composition of the Earth. *Chemical Geology* **120**, 223–253. [https://doi.org/10.1016/0009-2541\(94\)00140-4](https://doi.org/10.1016/0009-2541(94)00140-4).
- Melluso, L., Morra, V., Brotzu, P. & Mahoney, J. (2001). The cretaceous igneous province of Madagascar: geochemistry and petrogenesis of lavas and dykes from the central–western sector. *Journal of Petrology* **42**, 1249–1278. <https://doi.org/10.1093/petrology/42.7.1249>.
- Melluso, L., Morra, V., Brotzu, P., Franciosi, L., Grifa, C., Lustrino, M., Morbidelli, P., Riziky, H. & Vincent, M. (2007a). The Cenozoic alkaline magmatism in central-northern Madagascar: a brief overview. *Periodico di Mineralogia* **76**, 169–180.

- Melluso, L., Morra, V., Riziky, H., Veloson, J., Lustrino, M., Del Gatto, L. & Modeste, V. (2007b). Petrogenesis of a basanite–tephrite–phonolite volcanic suite in the Bobaomby (Cap d'Ambre) peninsula, northern Madagascar. *Journal of African Earth Sciences* **49**, 29–42. <https://doi.org/10.1016/j.jafrearsci.2007.06.002>.
- Moldoveanu, G. A. & Papangelakis, V. G. (2012). Recovery of rare earth elements adsorbed on clay minerals: I. Desorption mechanism. *Hydrometallurgy* **117–118**, 71–78.
- Moldoveanu, G. A. & Papangelakis, V. G. (2013). Recovery of rare earth elements adsorbed on clay minerals: II. Leaching with ammonium sulfate. *Hydrometallurgy* **131–132**, 158–166. <https://doi.org/10.1016/j.hydromet.2012.10.011>.
- Moldoveanu, G. A. & Papangelakis, V. G. (2016). An overview of rare-earth recovery by ion-exchange leaching from ion-adsorption clays of various origins. *Mineralogical Magazine* **80**, 63–76. <https://doi.org/10.1180/minmag.2016.080.051>.
- Möller, V. & Williams-Jones, A. E. (2016a). Petrogenesis of the Nechalacho Layered Suite, Canada: magmatic evolution of a REE–Nb-rich Nepheline Syenite Intrusion. *Journal of Petrology* **57**, 229–276. <https://doi.org/10.1093/ptrology/egw003>.
- Möller, V. & Williams-Jones, A. E. (2016b). Stable and radiogenic isotope constraints on the magmatic and hydrothermal evolution of the Nechalacho Layered Suite, northwest Canada. *Chemical Geology* **440**, 248–274. <https://doi.org/10.1016/j.chemgeo.2016.07.010>.
- Neave, D. A., Fabbro, G., Herd, R. A., Petrone, C. M. & Edmonds, M. (2012). Melting, differentiation and degassing at the Pantelleria volcano, Italy. *Journal of Petrology* **53**, 637–663. <https://doi.org/10.1093/ptrology/egr074>.
- Nougier, J., Cantagrel, J. & Karche, J. (1986). The Comores archipelago in the western Indian Ocean: volcanology, geochronology and geodynamic setting. *Journal of African Earth Sciences* **5**, 135–145.
- Oberti, R., Cannillo, E. & Toscani, G. (2012). How to name amphiboles after the IMA2012 report: rules of thumb and a new PC program for monoclinic amphiboles. *Periodico di Mineralogia* **81**, 257–267.
- Ódri, Á., Harris, C. & Le Roux, P. (2020). The role of crustal contamination in the petrogenesis of nepheline syenite to granite magmas in the Ditrău complex, Romania: evidence from O-, Nd-, Sr- and Pb-isotopes. *Contributions to Mineralogy and Petrology* **175**, 100. <https://doi.org/10.1007/s00410-020-01738-5>.
- Papini, M. & Benvenuti, M. (2008). The Toarcian–Bathonian succession of the Antsiranana Basin (NW Madagascar): Facies analysis and tectono-sedimentary history in the development of the East Africa-Madagascar conjugate margins. *Journal of African Earth Sciences* **51**, 21–38. <https://doi.org/10.1016/j.jafrearsci.2007.11.003>.
- Pfaff, K., Krumrei, T., Marks, M., Wenzel, T., Rudolf, T. & Markl, G. (2008). Chemical and physical evolution of the 'lower layered sequence' from the nepheline syenitic Ilímaussaq intrusion, South Greenland: implications for the origin of magmatic layering in peralkaline felsic liquids. *Lithos* **106**, 280–296. <https://doi.org/10.1016/j.lithos.2008.07.018>.
- Ponader, C. W. & Brown, G. E. (1989a). Rare earth elements in silicate glassmelt systems: I. Effects of composition on the coordination environments of La, Gd, and Yb. *Geochimica et Cosmochimica Acta* **53**, 2893–2903. [https://doi.org/10.1016/0016-7037\(89\)90166-X](https://doi.org/10.1016/0016-7037(89)90166-X).
- Ponader, C. W. & Brown, G. E. (1989b). Rare earth elements in silicate glassmelt systems: II. Interactions of La, Gd, and Yb with halogens. *Geochimica et Cosmochimica Acta* **53**, 2905–2914. [https://doi.org/10.1016/0016-7037\(89\)90167-1](https://doi.org/10.1016/0016-7037(89)90167-1).
- Rakotovoava, A. P., Jessell, M., Salvi, S., Béziat, D., Montel, J.-M. & Rakotondrazafy, M. (2014). The Ianapera-Ampanihy suture, SW Madagascar: a major tectonic boundary on the eastern margin of the Mozambique belt. *Journal of African Earth Sciences* **94**, 31–44. <https://doi.org/10.1016/j.jafrearsci.2013.12.009>.
- Riishuus, M. S., Peate, D. W., Tegner, C., Wilson, J. R. & Brooks, C. K. (2008). Petrogenesis of cogenetic silica-oversaturated and -undersaturated syenites by periodic recharge in a crustally contaminated magma chamber: the Kangerlussuaq intrusion, East Greenland. *Journal of Petrology* **49**, 493–522. <https://doi.org/10.1093/ptrology/egm090>.
- Rocco, I., Lustrino, M., Zanetti, A., Morra, V. & Melluso, L. (2013). Petrology of ultramafic xenoliths in Cenozoic alkaline rocks of northern Madagascar (Nosy Be Archipelago). *Journal of South American Earth Sciences* **41**, 122–139. <https://doi.org/10.1016/j.jsames.2012.06.012>.
- Rocco, I., Zanetti, A., Melluso, L. & Morra, V. (2017). Ancient-depleted and enriched mantle lithosphere domains in northern Madagascar: geochemical and isotopic evidence from spinel-to-plagioclase-bearing ultramafic xenoliths. *Chemical Geology* **466**, 70–85. <https://doi.org/10.1016/j.chemgeo.2017.05.016>.
- Ruan, C., Jun, T., Zhongjun, L., Cui, P., Yuanxin, W., Shirong, L., Cunwen, W. & Zhiang, Z. (2005). Existing state and partitioning of rare earth on weathered ores. *Journal of Rare Earths* **23**, 756.
- Salvi, S. & Williams-Jones, A. E. (1996). The role of hydrothermal processes in concentrating high-field strength elements in the Strange Lake peralkaline complex, northeastern Canada. *Geochimica et Cosmochimica Acta* **60**, 1917–1932. [https://doi.org/10.1016/0016-7037\(96\)00071-3](https://doi.org/10.1016/0016-7037(96)00071-3).
- Salvi, S. & Williams-Jones, A. (2006). Alteration, HFSE mineralisation and hydrocarbon formation in peralkaline igneous systems: insights from the Strange Lake Pluton, Canada. *Lithos* **91**, 19–34. <https://doi.org/10.1016/j.lithos.2006.03.040>.
- Sanematsu, K. & Watanabe, Y. (2016). Characteristics and genesis of ion adsorption-type rare earth element deposits. *Reviews in Economic Geology* **18**, 55–79.
- Schonenberger, J. & Markl, G. (2008). The magmatic and fluid evolution of the Motzfeldt intrusion in South Greenland: insights into the formation of Agpaitic and Miaskitic rocks. *Journal of Petrology* **49**, 1549–1577. <https://doi.org/10.1093/ptrology/egm037>.
- Schorscher, H. & Shea, M. (1992). The regional geology of the Poços de Caldas alkaline complex: mineralogy and geochemistry of selected nepheline syenites and phonolites. *Journal of Geochemical Exploration* **45**, 25–51. [https://doi.org/10.1016/0375-6742\(92\)90121-N](https://doi.org/10.1016/0375-6742(92)90121-N).
- Siegel, K., Williams-Jones, A. E. & van Hinsberg, V. J. (2017). The amphiboles of the REE-rich A-type peralkaline Strange Lake pluton—fingerprints of magma evolution. *Lithos* **288–289**, 156–174. <https://doi.org/10.1016/j.lithos.2017.07.012>.
- Siegel, K., Vasyukova, O. V. & Williams-Jones, A. E. (2018). Magmatic evolution and controls on rare metal-enrichment of the Strange Lake A-type peralkaline granitic pluton, Québec-Labrador. *Lithos* **308–309**, 34–52. <https://doi.org/10.1016/j.lithos.2018.03.003>.
- Smith, M. P., Moore, K., Kavecsánszki, D., Finch, A. A., Kynicky, J. & Wall, F. (2016). From mantle to critical zone: a review of large and giant sized deposits of the rare earth elements. *Geoscience Frontiers* **7**, 315–334. <https://doi.org/10.1016/j.gsf.2015.12.006>.
- Sun, S.-S. & McDonough, W. F. (1989). Chemical and isotopic systematics of oceanic basalts: implications for mantle composition and processes. *Geological Society, London, Special Publications* **42**, 313–345. <https://doi.org/10.1144/GSL.SP.1989.042.01.19>.
- Thomas, R. J., De Waele, B., Schofield, D. I., Goodenough, K. M., Horstwood, M., Tucker, R., Bauer, W., Annells, R., Howard,

- K., Walsh, G., Rabarimanana, M., Rafahatelo, J. M., Ralison, A. V. & Randriamananjara, T. (2009). Geological evolution of the Neoproterozoic Bemarivo Belt, northern Madagascar. *Precambrian Research* **172**, 279–300. <https://doi.org/10.1016/j.precamres.2009.04.008>.
- Tian, J., Tang, X., Yin, J., Luo, X., Rao, G. & Jiang, M. (2013). Process optimization on leaching of a lean weathered crust elution-deposited rare earth ores. *International Journal of Mineral Processing* **119**, 83–88. <https://doi.org/10.1016/j.minpro.2013.01.004>.
- Troll, V. R., Walter, T. R. & Schmincke, H.-U. (2002). Cyclic caldera collapse: piston or piecemeal subsidence? Field and experimental evidence. *Geology* **30**, 135–138. [https://doi.org/10.1130/0091-7613\(2002\)030<0135:CCPOP>2.0.CO;2](https://doi.org/10.1130/0091-7613(2002)030<0135:CCPOP>2.0.CO;2).
- Tucker, R. D., Conrad, J., Key, R. M., Pitfield, P. E. J., Randriamananjara, T., Taylor, C. D., Goodenough, K. M. & Thomas, R. J. (2008)  $^{40}\text{Ar}/^{39}\text{Ar}$  geochronology of Mesozoic and younger igneous rocks. In: BGS-USGS-GLW (Ed.) *Republique de Madagascar Ministère de L'Energie et des Mines (MEM/SG/DG/UCP/PGRM)*. British Geological Survey Research Report, 78. Keyworth, Nottingham.
- US Geological Survey (2022) *2022 Final List of Critical Minerals Federal Register / Vol. 87, No. 37*.
- Vasyukova, O. & Williams-Jones, A. E. (2016). The evolution of immiscible silicate and fluoride melts: implications for REE ore-genesis. *Geochimica et Cosmochimica Acta* **172**, 205–224. <https://doi.org/10.1016/j.gca.2015.09.018>.
- Vasyukova, O. & Williams-Jones, A. E. (2019). Tracing the evolution of a fertile REE granite by modelling amphibole-melt partitioning, the Strange Lake story. *Chemical Geology* **514**, 79–89. <https://doi.org/10.1016/j.chemgeo.2019.03.030>.
- Vasyukova, O. & Williams-Jones, A. E. (2020). Partial melting, fractional crystallisation, liquid immiscibility and hydrothermal mobilisation—a 'recipe' for the formation of economic A-type granite-hosted HFSE deposits. *Lithos* **356–357**, 105300. <https://doi.org/10.1016/j.lithos.2019.105300>.
- Wit, M. J.D. (2003). MADAGASCAR: heads it's a continent, tails it's an island. *Annual Review of Earth and Planetary Sciences* **31**, 213–248. <https://doi.org/10.1146/annurev.earth.31.100901.141337>.
- Xu, C., Kynický, J., Smith, M. P., Kopriva, A., Brtnický, M., Urubek, T., Yang, Y., Zhao, Z., He, C. & Song, W. (2017). Origin of heavy rare earth mineralization in South China. *Nature Communications* **8**, 14598. <https://doi.org/10.1038/ncomms14598>.
- Zhukova, I. A., Stepanov, A. S., Jiang, S.-Y., Murphy, D., Mavrogenes, J., Allen, C., Chen, W. & Bottrill, R. (2021). Complex REE systematics of carbonatites and weathering products from uniquely rich Mount Weld REE deposit, Western Australia. *Ore Geology Reviews* **139**, 104539. <https://doi.org/10.1016/j.oregeorev.2021.104539>.